Impact of fluidic flow on the development of the vasculature niche in IPSC-derived bone marrow organoids

Jamie Logsdon

MSc by Research

University of York

Biology

November 2025

Abstract

B-cell acute lymphoblastic leukaemia (B-ALL) is a haematological disease that affects both adults and children. In adults, although the initial remission rate is high, the main cause of deaths is due to relapse. It has been previously demonstrated that the bone marrow microenvironment plays an important role in this relapse in adults. Co-Cultures of B-ALL cells and Mesenchymal stromal cells (MSCs), as well as patient derived xenografts (PDX) have been used to demonstrate the importance of the bone marrow microenvironment in resistance to chemotherapies such as cytarabine (AraC). However, these models are not fully representative. Khan et al designed a 3D organoid model that allowed for B-ALL engraftment to model haematological diseases. This created a more complex model that included mesenchymal stromal cells (MSCs) and a sinusoidal-like vasculature. However, there were still limitations due to the vasculature produced being disconnected and non-functioning. Fluidic flow and shear stress has been shown to influence angiogenesis and vasculature production. We hypothesised that the addition of the fluidic flow would improve the vasculature within the bone marrow organoids. We found that applying a flow of 40µl/min did influence the vasculature with a decrease in vessel percentage area and junction density, whilst an increase in average vessel diameter. We concluded that the addition of fluidic flow decreased angiogenesis within the flow treated organoids but suggested the formation of a different vessel type. Further experiments with a range of flow rates would need to be performed that represent the flow and shear stress of different vessel types to make a more informed conclusion.

Declaration

I declare that this thesis is a presentation of original work and I am the sole author. This work has not previously been presented for a degree or other qualification at this University or elsewhere. All sources are acknowledged as references. All experiments were performed by the author unless otherwise stated.

Acknowledgments

Firstly, I would like to thank my supervisor Professor Adele Fielding for her continuous support throughout this project and beyond. I would also like to thank the whole Fielding lab of Juma, Jenny and Lucas that made this master's the best experience. I would especially like to thank Juma for training me throughout my masters in organoid culture and imaging hopefully I will be his favourite master's student. Additionally, I would like to thank Callum for all his help in the design of the microfluidic device and having the commitment to the project of being hit by a car and still making our first meeting. Finally, I would like to thank my parents who have been there for me since birth.

Table of Contents

Abstract *2*

Declaration *3*

Acknowledgments *4*

List of Figures *6*

List of Tables *7*

Introduction *7*

Bone Marrow Microenvironment **7**

B-cell Acute Lymphoblastic Leukaemia (B-ALL) **8**

B-ALL microenvironment **9**

Organoid Overview **10**

Organoids 10

Bone marrow organoids 11

Vascular endothelial cells **14**

Angiogenesis **14**

Fluidic flow and shear stress **15**

Fluidic flow 15

Interstitial flow 16

Blood flow 16

Shear stress and its signalling pathways 16

Gene expression due to flow and shear stress 17

Effect of fluidic flow and shear stress on angiogenesis 17

Addition of fluidic flow to an organoid system 18

Methods for studying vasculature in organoids **18**

Hypothesis and aims **19**

Methods *20*

Cell culture **20**

Induced Pluripotent Stem Cell (IPSC) culture 20

Cell line culture 20

Microfluidics **21**

Microfluidic chip fabrication 21

Organoids **23**

Organoid differentiation 23

Combined organoid protocol 23

Engraftment of acute lymphoblastic leukaemia cells into the organoid 24

Fluidic flow 24

Imaging **25**

Whole mount imaging 25

Cryosectioning 27

Immunostaining 27

Angiotool analysis 28

Flow cytometry **29**

Organoid dissociation 29

Cell viability and apoptosis assay 30
Endothelial cell count 30
Cloning 30
Primer design 30
PCR 32
Results 33
Optimising vessel staining 33
Whole mount imaging 33
Cryosections 34
Baseline distribution of ALL cells within bone marrow organoids 36
Analysis of vasculature in organoids 38
Evaluating angiotool: response of the bone marrow organoids vasculature to cytarabine treatment 42
Optimising dissociation of organoids flow cytometry analysis 43
Design of microfluidic chip and system 44
Optimising chip design 44
Optimising fluidic system 48
Elimination of bubbles 50
Effect of fluidic flow on the vasculature 54
Viability of flow vs static 54
Changes in the vasculature under fluidic flow 55
Effect of fluidic flow on engraftment of ALL in bone marrow organoids 61
Modifying IPSC to allow label-free analysis of the vasculature using RFP under control of VE-cadherin promoter 62
Discussion 65
Appendix 72
Abbreviations 74
References 75

List of Figures

Figure 1. CAD design of the initial microfluidic chip 22
Figure 2. Angiotool ImageJ plugin default parameter settings 29
Figure 3. Plasmid sequencing used for primer design. 31
Figure 4. Optimisation of antibody staining. 36
Figure 5. Engraftment of ALL cells in organoids. 38
Figure 6. Vessel analysis methods. 41
Figure 7. Treatment with AraC influences the vasculature within bone marrow organoids. 42
Figure 8. Viability of organoids is highest using shaking incubator for dissociation. 44

Figure 9. Initial chip design and casing evolution. 45
Figure 10. Flow-cytometric determination of the viability of fluidic flow organoids increased with new microfluidic chip design. 47
Figure 11. Addition of a bubble trap does not improve the viability of bone marrow organoids. 50
Figure 12. Bubbles formed within the microfluidic chip designs. 54
Figure 13. Flow treated organoids are as viable as the control organoids. 55
Figure 14. Fluidic flow inhibits vasculature growth in organoids. 60
Figure 15. The use of fluidic flow does not improve engraftment of ALL cells in bone marrow organoids. 62
Figure 16. Gel electrophoresis confirms backbone primer is producing incorrect product. 65

List of Tables

Table 1. Differences in cytokines and growth factors added in each phase of the protocol 13
Table 2. Outputs of angiotool analysis 19
Table 3. Cell lines 20
Table 4. Phases of media needed for organoid generation 25
Table 5. List of primary and secondary antibodies, lectins and dyes used in immunostaining of whole mount and cryosections and flow cytometry 26
Table 6. Primer sequences for plasmid design 31
Table 7. Approaches to eliminate bubbles from microfluidic system 51

Introduction

Bone Marrow Microenvironment

Bone marrow is a primary lymphoid tissue and haematopoietic organ that is responsible for the production of erythrocytes, granulocytes, monocytes, lymphocytes and platelets (Travlos, 2006). The bone marrow microenvironment (BMM) is characterized by a complex architecture, enriched with arterioles and sinusoidal vessels, and an array of regulatory signals that contribute to the fate of mesenchymal stromal cells (MSCs), haematopoiesis and B-cell development. Within this microenvironment is the haematopoietic stem cell (HSC) niche, which can be further divided into two functionally distinct compartments: the central niche and endosteal niche. The endosteal niche consists of osteoblasts, osteocytes and transition zone vessels that connect the arterioles to the sinusoids

(Méndez-Ferrer et al., 2020) and is located close to the surface of the bone. Osteoblasts secrete chemokines and growth factors, including CXCL12, granulocyte colony-stimulating factor (G-CSF) and thrombopoietin (TPO), that all play critical roles in the regulation of HSC homing and quiescence. Osteocytes, the differentiated form of osteoblasts, do not directly regulate HSC behaviour, instead they indirectly modulate HSCs through osteoblast function (Galan-Diez et al., 2018). The central niche is composed primarily of vascular structures surrounded by the perivascular mesenchymal stem/progenitor cells (MPSCs). Mesenchymal stromal cells (MSCs) are a trilineage progenitor population with the capacity to differentiate into osteoblasts, adipocytes and chondrocytes. CXCL12 is a chemokine secreted by MPSC and depletion of CXCL12 in PRX1-Cre-expressing stromal cells resulted in impaired B lymphopoiesis, demonstrating that MPSC-derived cytokines are essential for supporting B cell development (Hughes et al., 2022).

Sinusoidal and arteriole vessels comprise most of the central niche. They are formed from endothelial cells and regulate exchange of cells, nutrients, soluble factors, oxygen and waste between the BMM and peripheral blood. The vasculature can be characterized by expression of surface markers such as CD31. Transition zone vessels (type H), which are directly connected to the arterioles, have high CD31, whilst sinusoidal vessels (Type L) have low CD31 (Hughes et al., 2022). Endothelial cells can regulate lymphopoiesis through signalling pathways including the Notch, which in turn regulates early haematopoietic progenitors. The BMM often plays a role in malignancies, with disruptions to haematopoiesis influencing the development and progression of many myeloid and lymphoid diseases. Therefore, understanding these complex interactions within are essential for developing novel therapeutics (Galan-Diez et al., 2018).

B-cell Acute Lymphoblastic Leukaemia (B-ALL)

B-cell acute lymphoblastic leukaemia (B-ALL) is a blood cancer, characterised by proliferation of the immature lymphoid cells in the bone marrow. There are genetic subtypes of B-ALL that are associated with a number of genetic lesions, many of which are balanced chromosome translations such as BCR:ABL, (Huang et al., 2020b) which is the most common fusion gene in adult B-ALL. The incidence of B-ALL is biphasic with a

high prevalence in childhood and another again in late adulthood (Dores et al., 2012). The survival rate of B-ALL decreases with age. Children have a significantly higher survival rate (85%) compared to adults (30-40%) (Roberts, 2018). Initially, newly diagnosed adult patients have a high remission rate with standard treatment. However, the major cause of death is adults is due to relapse which has a poor prognosis (Fielding et al., 2007), with 30-60% of adult patients experiencing relapse (Roberts, 2018). Survival rates are improving with new treatments such as blinatumomab (Litzow et al., 2024). Why all adult B-ALL have a worse outcome than paediatric B-ALL is not fully understood – the range of genetic lesions tends to be quite distinct (Roberts, 2018). The mechanism by which these different genetic lesions impact prognosis is not understood.

B-ALL microenvironment

The role of the bone marrow microenvironment and mesenchymal stromal cells in B-ALL chemoresistance and relapse is beginning to be understood. In 2014, it was demonstrated that reactive oxygen species (ROS)-inducing chemotherapies such as cytarabine (AraC) induced the development of a chemoprotective mesenchymal stromal cell (MSC) niche, composed of nestin- and α-smooth muscle actin-expressing (α-SMA) cells (Duan et al., 2014).

Polak *et al* showed the formation of tunnelling nanotubes (TNTs), which are membranous cytoplasmic connections, between MSCs and B-ALL cells using confocal microscopy (Polak et al., 2015). B-ALL cells use the TNTs to communicate with MSCs and these signals result in the secretion of pro-survival cytokines such as IL-8, CXCL10 and CCL2 into the microenvironment to assist with B-ALL survival. They also showed that intercellular mitochondrial transfer occurred and led to chemoresistance to prednisone. In 2016, Ebinger *et al*, using patient derived xenograft (PDX) mouse models, developed a model of minimal residual disease (MRD), characterized by persistent, bone marrow resident, chemoresistant and quiescent B-ALL cells (Ebinger et al., 2016). This phenotype was then shown to be reversible, since the removal of the cells from their niche led to chemosensitivity and reduction in disease burden.

The role of intercellular mitochondrial transfer was investigated further by the Fielding lab, where it was shown that mitochondria could be donated to ALL cells by MSC via tunnelling nanotubes (Burt et al., 2019). Depleting MSC mitochondria with a low-dose

ethidium bromide culture led to reduced chemoprotection under co-culture conditions. Exposure to AraC activated the MSCs to become cancer associated fibroblasts (CAFs). CAFs were identified by the upregulation of a panel of CAF-associated genes, including the cytokines and chemokines IL-6, IL-8 and CCL2; growth factors and genes involved in cytoskeletal remodelling. These cells had morphological changes with profound actin stress fibres.

Further investigation by the Fielding lab showed that the CAF development can occur not only in response to chemotherapy but also by exposure to some genetic subtypes of ALL themselves (Burt et al., 2024). This occurred in a contact-independent manner, with exposure to ALL-cell conditioned media being sufficient. This depended on mitochondrial-derived double stand RNA (mt-dsRNA) being released into the conditioned media. The mechanism of release and uptake of mitochondria by the MSCs is currently unknown. However, this finding indicated that the B-ALL cells can remodel their microenvironment into a protective niche in the absence of chemotherapy, which may have important implications for relapse. A recent paper by the Mullighan group showed that MSC interaction with B-ALL cells increase survival and chemoresistance through an integrin β1 interaction (Park et al., 2023). Whilst *in vitro* models in the use of cell lines or *in vivo* models are commonly used to investigate these interactions, they are limited in terms of their lack of cell-cell interactions and murine microenvironment respectively (Skelding et al., 2025). Therefore, it is important to look at the use of new models to investigate the B-ALL microenvironment.

Organoid Overview

Organoids

The primary models for biological research are animals and 2D cell cultures. This has allowed scientist to research disease pathways, mechanisms and drug targets, expanding and improving the biological field dramatically. However, there are limitations. Animal models are not fully representative of humans, creating difficulties in drug discoveries (Pritt and Hammer, 2017). Conversely 2D cell cultures lack the cell-cell interaction due to their limited cell diversity and makes it problematic to mimic the cellular mechanisms present in more complex tissues (Tang et al., 2022).

In 1971, Sutherland *et al* developed a spheroid model from hamster lung cells to model nodules seen in patients with carcinomas (Sutherland et al., 1971). Spheroids are generated from the spontaneous aggregation of cells. They can be cultured with or without the support of extracellular matrix (ECM). They can be generated relatively easily and quickly with the simplest method being the pellet culture, where centrifugation helps promote cell-cell adhesion (Gunti et al., 2021). Organoids are *in vitro* 3D models that contain multiple cell types and complex structures to allow them to function as specific *in vivo* tissues. Organoids can either be induced pluripotent stem cell (iPSC) derived or tissue derived. Induced pluripotent stem cells (iPSCs) are being widely used in biological research due to their capability to become any cell type (Cerneckis et al., 2024). Induced pluripotent stem cell (iPSC) derived organoids are generated by expanding an undifferentiated population of human IPSCs on an extracellular matrix such as Matrigel or synthetic hydrogels, to create aggregates. Tissue-derived organoids involve a tissue biopsy that can be dissociated to obtain a starting population which can be, for example, normal stem/progenitor cells, differentiated cells or cancer cells. The starting population is important as it affects the function of the tissue to be mimicked, so tissue resident stem/progenitor/differentiated cells are obtained for tissue-derived organoids (Zhao et al., 2022). Cancer organoids can be generated from many types of tumours. Tumour cells are embedded into a Matrigel and cultured in media supplemented with specific cytokines and growth factors for the designated tissue type such as fibroblast growth factor (FGF), bone morphogenetic protein (BMP) and glycogen synthase kinase 3 (GSK3) inhibitor (CHIR99021). Unfortunately, these don't include additional stomal cells or immune cells that are important in the response to external factors like immunotherapies, displaying the importance of complex organoids that include multiple cell types (Polak et al., 2024).

Bone marrow organoids

Two groups recently developed IPSC-derived bone marrow organoids that allow for the study of haematological disorders such as B-ALL. Khan *et al* (Khan et al., 2023) produced a model of bone marrow over a 13-day procedure through the addition of specific cytokines of FGF2, FLT3, BMP4 and culture in hypoxia for mesodermal induction (Khan et

al., 2023). They analysed the organoids by flow cytometry, immunofluorescence and single-cell RNA sequencing (scRNAseq) and through transmission electron microscopy to identify the distinct cell populations and structures within the organoid. The organoids contained endothelial cells in the form of lumen-forming sinusoidal vessels that were characterized by the increased expression of FLT4, the encoding gene for the growth factor VEGFR3. Vascularisation was optimized by the addition of type I and IV collagen to the hydrogel where the density of CD34 and CD144 endothelial cells was significantly increased compared to the collagen IV hydrogel only. Single-cell RNA sequencing (scRNAseq) demonstrated the organoids contained HSPC, erythroid cells, neutrophils, monocytes, megakaryocytes, eosinophils, fibroblasts, endothelial cells and MSCs. This model can support proliferation of B-ALL patient-derived xenografts. Although this model is a clear advance upon 2D models, it currently does not contain the osteoid lineage, lymphoid cells and adipocytes. Additionally, the vasculature within the organoid does not seem to contain the subtypes of sinusoidal and arteriole endothelial cells. It was suggested that the addition of a dynamic flow could result in a more physiologically representative bone marrow model (Khan et al., 2023).

Frenz-Wiessner *et al* also produced a bone marrow organoid with similar properties in the sinusoidal-like vasculature, MSCs and neutrophils (Frenz-Wiessner et al., 2024). After 17 days, they had produced bone marrow organoids with a mean diameter of 1300µm. They used flow cytometry to determine the different populations present within the organoids displaying three main populations of haematopoietic (CD45+), endothelial (CD45- CD31+) and MSCs (CD45-CD31-CD271+). Transmission electron microscopy was used to confirm the presence of hematopoietic cells in the lumen of the vessels. There are also limitations with this model. Due to the relative cellular immaturity this model is more representative of a fetal bone marrow than an adult marrow. By contrast to Khan et al, this model has the potential for multilineage haematopoietic compartments and the differentiation of the endothelial cell subtypes due to the differences in protocols, including activation of Wnt signalling by CHIR99021 and inhibition of activin/nodal-signalling through SB431542 (Table 1), which was seen in the scRNA-seq data (Frenz-Wiessner et al., 2024). The table below summarises the main differences between the models.

Table 1. Differences in cytokines and growth factors added in each phase of the protocol

Phase	Khan et al	Phase	Frenz-Wiessner et al
1 (Day 0-3) - Mesodermal induction	Base media: APEL 2 Cytokines: BMP4, FGF2, VEGFA	1 (Day 0-2) – Mesodermal induction	Base media: mTeSRplus Supplement: CHIR99021 Cytokines: VEGF, BMP4
2 (Day 3-5) – Vascular committment	Base media: APEL2 Cytokines: BMP4, FGF2, VEGFA, hSCF, Flt3	2 (Day 2-6) – Hemogenic endothelial induction	Base media: Essential6, change to Stempro-34 on day 4 Supplement: SB431542 Cytokines: bFGF, VEGF, SCF
3 (Day 5-12) – Vascular spouting	Base media: APEL 2 Cytokines: VEGFA, VEGFC, FGF2, BMP4, hSCF, Flt3, EPO, TPO, G-CSF, IL3, IL6	3 (Day 6-10) – Vascular sprouting	Base media: Stempro-34 Cytokines: IL3, Flt3L, TPO, VEGF, SCF (on day 8 SCF concentration decreased)
4 (Day 12+) – Collection of organoids into 96 well plate	Base media: APEL 2 Cytokines: VEGFA, VEGFC, FGF2, BMP4, hSCF, Flt3, EPO, TPO, G-CSF, IL3, IL6	4 (Day 10-17) – Collection and maturation	Base media: Stempro-34 Cytokines: IL3, Flt3L, TPO, VEGF, low SCF

Vascular endothelial cells

The cardiovascular and lymphatic systems are involved in the transport of oxygen, small molecules, nutrients around the body, and maintaining fluid balance, defending against pathogens and absorbing fats respectively. They are made up of a vascular network that is critical for the survival of cells throughout the body. The key component of these vessels are endothelial cells. During development, blood vessels arise through vasculogenesis, which is tightly regulated by vascular endothelial growth factor (VEGF) and Notch signalling (Trimm and Red-Horse, 2023). There is high heterogeneity within endothelial cells - they form four major vessel groups within the body: arterial, venous, capillary and lymphatic. Arterial endothelial cells carry oxygenated blood away from the heart and have thick walls to withstand the force of high flow rates, whilst venous endothelial cells transport deoxygenated blood and therefore have much thinner walls. Capillaries have an extremely thin endothelial cell lining to allow for effective exchange of oxygen and nutrients, with a very slow flow rate. Lymphatic endothelial cells take part in the immune response and have a discontinuous basement membrane to allow for immune cell entry (Przysinda et al., 2020). The organization within the vascular network follows a hierarchy from arteries to a comprehensive capillary network leading to veins. Two distinct bone capillary subtypes have been identified through marker expression and functional characteristics. Type H capillaries that are found in the endosteal niche in the bone, have high expression of the junctional protein PECAM1/CD31 and sialoglycoprotein endomucin (EMCN). These vessels appear tightly packed and receive blood from the arteries. Comparatively, the L type vessels that correspond to sinusoidal vessels have a low expression of CD31 and EMCN. They are in the central niche and surrounded by haematopoietic stem cells. L type vessels do not directly receive blood from the arteries but instead from the H type vessels (Sivaraj and Adams, 2016).

Angiogenesis

Angiogenesis is the process of creating new blood vessels and is an essential component to survival. Being a dynamic process, it is controlled by both pro- and anti-angiogenic molecules. The formation of a mature vasculature is important in regular

blood flow around the body to supply tissues with oxygen and nutrients (Liu et al., 2023b). VEGF is a key mediator in the highly regulated process that is angiogenesis, with its interactions stimulating the process of new vessel formations (Schneider et al., 2011). Additionally, Notch signalling plays a significant role in the regulation of angiogenesis (Akil et al., 2021). Throughout lymphatic development, Notch signalling is an important pathway involved in the development of the vasculature. However, it also inhibits angiogenesis through the repression of tip cell formation. Watson et al, found that the notch ligand dll4 was repressed by blood flow, with a loss of function leading to excessive and unusual angiogenesis (Watson et al., 2013). Further data indicated that the contribution of the blood flow to angiogenesis was highly context dependent, with it being crucial in a hypoxic condition but not in a normal condition (Watson et al., 2013).

Fluidic flow and shear stress

Fluidic flow

Throughout development, cells experience intracellular and extracellular forces that result from fluidic flow. Fluids provide an important way for the transport of nutrients and waste around the body. The type of fluidic flow can be determined by the Reynolds number. A large Reynolds number indicates higher velocities, higher densities and smaller viscosities, which results in turbulent flow. For example, in the heart a Reynolds number of less than one at most leads to an unsteady laminar flow. A small Reynolds number indicates slower velocities and higher viscosities, which results in a more controlled laminar flow (Freund et al., 2012). Within a biological circumstance there are multiple types of fluidic flow that can be generated. Transendothelial fluidic flow occurs in angiogenesis and can be generated using a fluid column *ex vivo*. Within microfluidic systems, a peristaltic pump is primarily used to generate interstitial and luminal flow. Peristaltic pumps have been shown to improve maturation and development of both liver and kidney organoids, through improved growth and development of key compartments respectively (Juste-Lanas et al., 2023).

Interstitial flow

Interstitial flow is produced by the movement of a fluid, which contains growth factors and chemokines, through the extracellular matrix. Interstitial flow also generates shear stress that causes physiological responses in cells (Yao et al., 2012). The shear stress that endothelial cells experience from interstitial flow is not widely understood but is considered a regulator of angiogenesis (Hu et al., 2022). Under a low interstitial flow rate (10μm/s), the shear stress generated can cause morphological changes in both lymphatic endothelial cells and blood endothelial cells. Ng *et al* compared cells within a static condition to those exposed to an interstitial flow. The endothelial cells that were exposed to flow formed a vascular network, whereas those under static conditions did not (Ng et al., 2004). Additionally, interstitial flow is involved in bone remodelling (You et al., 2001). Using a microfluidic chip, flow was applied to a spheroid model of periodontal ligament stem cells, resulting in an increase in osteodifferentiation (Mishra et al., 2023).

Blood flow

Blood flow varies significantly across the organs within the body depending on organ function, and its function can be affected by changes in blood flow. It is difficult to study the functional organisation of blood flow due to difficulties imaging intact bone. Using various imaging techniques of the blood flow, the velocities in different vessels were determined. Arterial vessels had the highest velocity of 1.95±0.57 mm/s and shear stress 65.5±16.0 dyn/cm^2, whilst sinusoidal capillaries had the lowest of 0.23±0.22 mm/s and 2.9±2.7 dyn/cm^2 (Bixel et al., 2017).

Shear stress and its signalling pathways

Shear stress is the force per unit area that is created when a tangential force (in this case, blood flow) acts on a surface (in this case, endothelial cells). Shear stress can influence signalling pathways through mechanotransduction. Endothelial nitric oxide synthase (NOS) is a mechanosensing protein that maintains vascular quiescence in response to shear stress (Yuan, 2019).

The activation of the signalling pathways mitogen-activated protein kinase (MAPK) and nitric oxide (NO) lead to the mechanotransduction of MSCs (Liu et al., 2010). Cellular

function can be affected by intracellular signals produced by endothelial cells that are activated by a fluidic shear stress. These signals are sensed by vascular growth factors (VEGF) and adhesion molecules such as platelet endothelial cell adhesion molecule-1 (PECAM1/CD31), that activate endothelial signalling pathways that involve the molecules MAPK, PI3K and protein kinase C (PKC) (Li et al., 2005). The MAPK pathway promotes cell proliferation in early-stage angiogenesis. This pathway can be activated by the binding of the pro-angiogenic factors VEGF and fibroblast growth factor (FGF) to receptors on MAPK and phosphorylated ERK, an output of the MAPK pathway (Song and Finley, 2018).

Gene expression due to flow and shear stress

Depending on the type of flow and shear stress applied to the endothelial cells, this determines the different genes that are expressed. A steady laminar shear stress increases expression of the genes OCT4 and AFP that leads to increased pluripotency. Whilst an oscillatory shear stress activates angiopoietin-2 (Ang-2) via the B-catenin/Wnt signalling pathway, which is critical in angiogenesis and vascular repair. Additionally, the VEGF-Notch signalling pathway, which is induced by shear stress, upregulates the arterial marker EphrinB2, whilst downregulating the venous marker Eph4 within a murine stem cell. A disturbed flow can activate the Notch1 pathways, which is involved in determining the type of vessel produced (Lee et al., 2015).

Effect of fluidic flow and shear stress on angiogenesis

The process of angiogenesis is not fully understood. It seems that the addition of a shear stress through blood flow reduces endothelial sprouting through the nitric oxide pathway, whilst interstitial flow induces sprouting (Song and Munn, 2011).

However, the literature variously describes fluidic flow as essential, unnecessary or even inhibitory on the production of new vessels through angiogenesis. Nicoli *et al*, described a genetic pathway in which the induction of *klf2a* activates VEGF signalling through flow that results in the remodelling of blood vessels, indicating blood flow induces angiogenesis (Nicoli et al., 2010). However, the expression of CXCR4 is reduced in the presence of blood flow resulting in reduced angiogenesis within the brain capillaries of

zebrafish, demonstrating the blood flow can be an inhibitor to vessel development (Bussmann et al., 2011).

Addition of fluidic flow to an organoid system

The emerging technology of microfluidics in biological research allows for an environment where fluidic flow can be controlled and have effects on nutrient supply, drug delivery and the production of 3D organ models with organoids on a chip (Saorin et al., 2023). Microfluidics have been used in models of the brain microvascular network, where interstitial flow was applied for 7 days and an increase in mean spout count, average length and average diameter increased with flow, inducting that interstitial flow increased blood endothelial cell angiogenesis (Winkelman et al., 2021). In 2019, Homan *et al* added an interstitial flow to kidney organoids and discovered improved vascularization and maturation (Homan et al., 2019). The organoids were placed into a microfluidic device for 10 days during the differentiation, with a flow rate of 1-4.27mL/min applied to generate a shear stress upon the organoids. They used the vessel analysis software angiotool (Zudaire et al., 2011) to conclude that fluidic flow is a key factor in increased vascularization of kidney organoids (Homan et al., 2019). This suggested that the findings may be transferable to other organoid models, such as the bone marrow organoid and forms part of the basis for this project.

Methods for studying vasculature in organoids

Organoids are 3D structures, so the use of whole mount imaging gives an overview of the entire vasculature, and the connections formed. However, the use of cryosections allows for a more detailed spatial understanding in a single plane. Flow cytometry is the most appropriate method for enumerating cells due to its high throughput.

Frenz-Weissner *et al*, and Homan *et al* both used a plugin on imageJ called angiotool to quantify different aspects of the vasculature (Frenz-Wiessner et al., 2024, Homan et al., 2019).

Angiotool provides multiple outputs (Table 2). A limitation to angiotool is that it does not output the individual lengths or diameters of each vessel. Nonetheless, it can be used to identify increased angiogenesis.

Table 2. Outputs of angiotool analysis

Output	Explanation
Explant area	the area containing the vessels
Vessel area	the area of the segmented vessels
Vessel Percentage area	the percentage area of vessels within the explant area
Total number of junctions	defined as where a new vessel branches
Junction Density	number of junctions normalised to the explant area
Total vessel length	distance of all vessels segmented
Average vessel length	total vessel length divided by number of vessels segmented
Average vessel diameter	total diameters together divided by number of vessels segmented

(Aschauer et al., 2024, Zudaire et al., 2011)

Hypothesis and aims

Hypothesis: The addition of fluidic flow during the development of bone marrow organoids will improve vascularisation through an increase in connected vessels within the organoid that can be tracked using the Fiji software angiotool.

Aims:

- To describe and characterise the vasculature within iPSC-derived bone marrow organoids
- To generate a microfluidic device to allow for the addition of fluidic flow to the bone marrow organoids
- To evaluate the effect of fluidic flow on the formation of vasculature network within a bone marrow organoid
- To determine the effect of fluidic flow on the distribution of ALL cells in the bone marrow organoids

Methods

Cell culture

Induced Pluripotent Stem Cell (IPSC) culture

IPSCs were cultured in 6 well plates coated with Geltrex (Fisher Scientific, 15180617) in StemFlex medium (Thermo Fisher Scientific, A3349401). Wells were coated with 2mL of Geltrex and incubated at 37ºC for 1 hour or at room temperature for at least 2 hours. Pre-coated plates were wrapped in parafilm and stored at 4ºC for up to 2 weeks. Once 70% confluent, iPSCs were passaged. For cell passaging, media was aspirated and wells washed with 1mL of phosphate buffered saline (PBS), before adding 1mL EDTA and incubating for 3 minutes at 37ºC. EDTA was removed and cells were gently dissociated in 2mL of StemFlex media using a P1000. Geltrex coating was removed from a fresh plate and 2mL of StemFlex media was added. Dissociated cells were seeded at ratio of 1:2 or 1:3. Media was replaced every other day.

Cell line culture

SD1 and SEM cells were grown in RPMI 1640 media with L-Glutamine supplemented with 10% fetal bovine serum (FBS) and 1% penicillin and streptomycin. Cells were maintained in a 75cm^2 tissue culture flask. For passaging, fresh media was added to a new 75cm^2 flask and cells were taken up and split at a 1:5 ratio. They were split once 70% confluent. Before experiments, cells were counted using trypan blue and a haemocytometer.

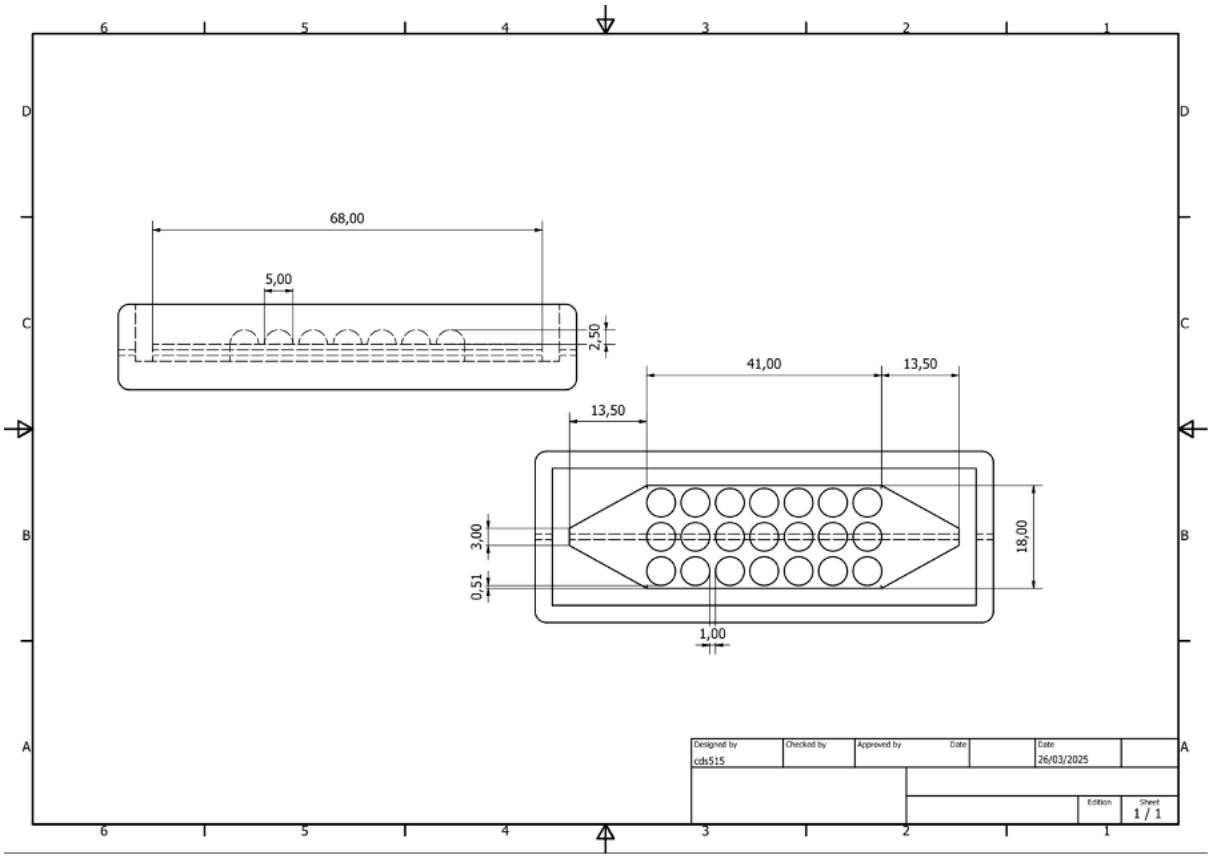
Table 3. Cell lines

Cell Line	Cell Type	Genetic Translocation	Accession Number
SD1	Pre B-ALL	BCR::ABL1	ACC-366
SEM	Pre B-ALL	KMT2A::AFF1	ACC-564
IPSC	Stem Cell	N/A	N/A

Microfluidics

Microfluidic chip fabrication

Using Tough2000 resin, a negative mould for Polydimethylsiloxane (PDMS) was printed on a FormLabs 3D printer (Figure 1). The PDMS channel was created using a SYLGARD® 184 kit (Sigma). SYLGARD was mixed at a 7:1 ratio of base: curing-agent and left in a vacuum chamber for 15 minutes to degas. Following this, 1mm pins were inserted into the 3Dprinted mould to create the inlet and outlet. The SYLGARD mixture was poured into a 3D mould and left in a vacuum chamber for a further 15 minutes to degas. Once all the bubbles were removed, the mould was placed into an oven at 65°C for 12 hours to cure. Once cured, the pins were removed, PDMS was cut out of the mould and stored at room temperature. The PDMS chip was autoclaved before use.



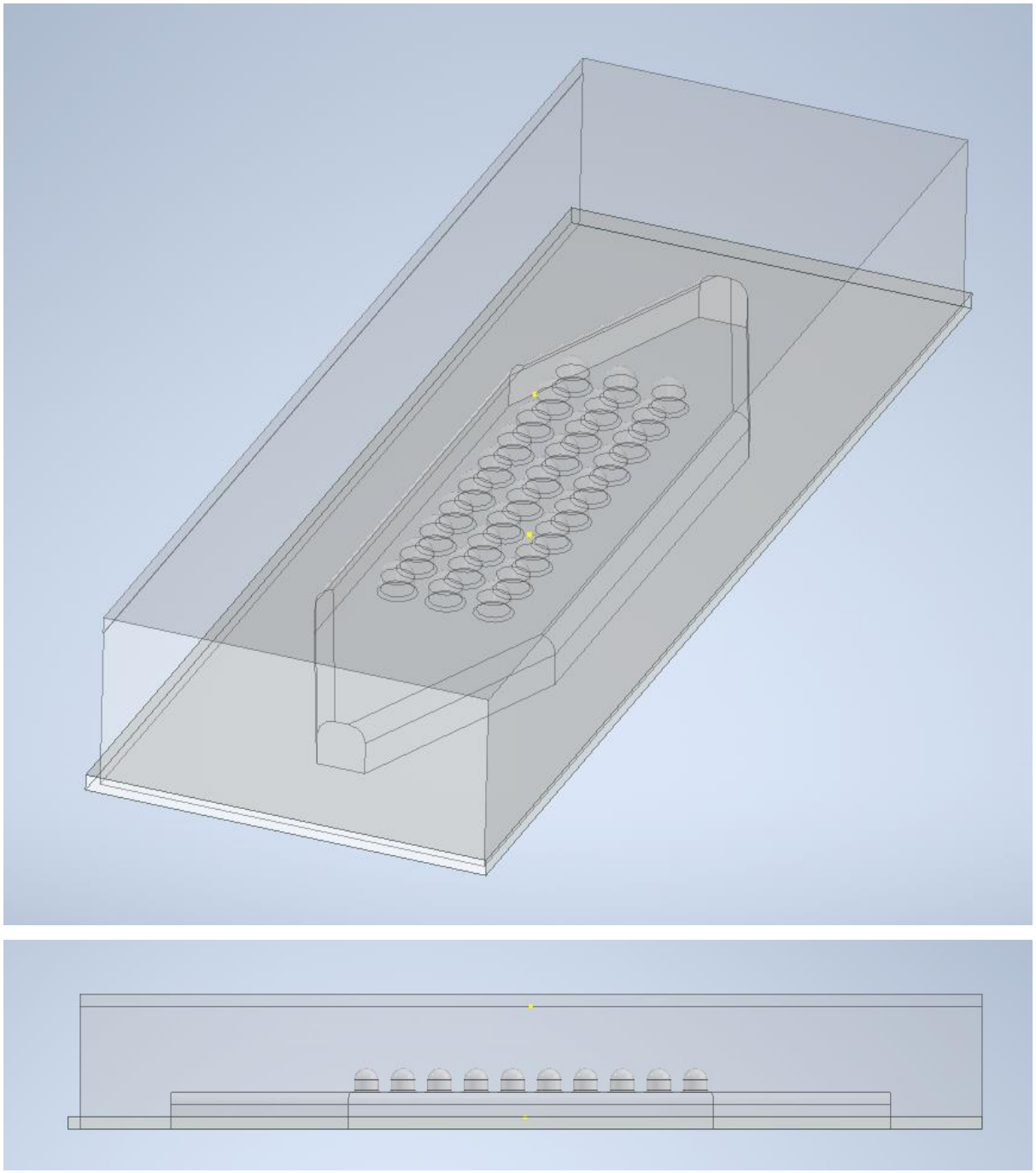


Figure 1. CAD design of the initial microfluidic chip

Generated by the Johnson team in the Department of Physics, Engineering and Technology at the University of York. The initial Chip design contained 30 round bottomed wells of 5x5x5mm. PDMS was inserted into the mould and cured to produce the microfluidic device.

Organoids

Organoid differentiation

Using organoids developed by Khan *et al* (Khan et al., 2023) and following the protocol by Olijink *et al (Olijnik et al., 2024)*, on day -1, IPSCs were dissociated from a 6 well plate containing Geltrex and transferred into an ultra-low attachment (ULA) 6 well plate in StemFlex media supplemented with Revita cell and were incubated for 24 hours at 37 °C. On day 0, aggregates were collected, centrifuged at 200g for 4 minutes and resuspended in phase I media (Table 4). Aggregates were placed back into the ULA plate and incubated for 3 days at 5% O_2 and 37°C in a hypoxic workstation. After 3 days, the aggregates were collected via gravitation and the media was replaced with phase II media (Table 4). They were incubated at normoxia (20% O_2) for 48 hours. On day 5, hydrogel containing 40% growth factor reduced Matrigel, 30% collagen I vitrocol diluent and 30% collagen I +IV mix was prepared on ice. A 12 well plate was primed with Phosphate-Buffered Saline (PBS), before the first layer of hydrogel was added and incubated at 37ºC for 90 minutes to polymerise. Aggregates were collected through gravitation; the media was removed, and aggregates were combined with the second layer of hydrogel. Roughly 30-40 aggregates were placed into each well and the hydrogel was polymerised for a further 90 minutes in the incubator, before phase III (A) media was added. On day 7, media was replaced with phase III(B) media and incubated for a further 72 hours. On day 10, 50% of the media was replaced with phase III (C) media. By day 13, the aggregates had fully differentiated into organoids and were removed from the hydrogel and placed into a 96 well plate in 100µl of phase IV media. Organoids were incubated for 24 hours and redistributed if needed. From this point onwards the media was changed at a ratio of 50:50.

Combined organoid protocol

The Khan lab developed a new protocol that additionally included the lymphoid lineage as well as the myeloid lineage present from the previous protocol (Shen et al., 2025). On day 5, a granular hydrogel was prepared on ice that contained 1200µl Matrigel, 800µl collagen type I + IV mix, 600µl VitroCol, 200µl Fibrinogen at 20mg/ml, 30µl 1N NaOH and 4U Thrombin (450U/ml) per seven 96 well plates of aggregates. The hydrogel was transferred into a sealed syringe and polymerised in the incubator for 90 minutes. The

hydrogel was diluted in 5mL of phase III (A) media and fragmented by passing it through a series of needles of increasing size. Roughly 120 aggregates were resuspended in the 5mL of granular hydrogel media. Using a multichannel pipette, the aggregates were distributed across the 96 well plate in 50µl of hydrogel media. On day 7, 50µl of phase III (B) media was added and 96 well plates were incubated at 37°C for 72 hours. Using a multichannel pipette, from day 10 onwards a 50:50 media change was done with phase III (C) media, being careful not to accidently remove any organoids. From day 13 onwards the protocol was the same. Whilst in this new protocol, the organoids are kept in 5% O_2 for 20 days, we continued to do just 3 days as in original protocol.

Engraftment of acute lymphoblastic leukaemia cells into the organoid

On day 14, either SD-1 or SEM cells were collected and counted using a haemacytometer. Cells were centrifuged, and pellets resuspended in phase IV media, with a total of 6000 cells per organoid in 100µl of media. A media change was done at a 50:50 ratio of old to new media. Organoids were then incubated at 37°C.

Fluidic flow

On day 5, individual aggregates were embedded in 25µl of hydrogel into the individual wells of the microfluidic device and placed into the incubator for 30 minutes to polymerise. Phase III (A) media was added to the microfluidic device using a syringe. Only the device and small rigid tubing was used on day 5. On day 7, phase III (A) media was replaced with phase III (B) media. Once the whole system had been primed with media, a clamp was placed on the end of the peristaltic tubing to avoid bubbles when the closed system was formed. The peristaltic tubing was attached to the peristaltic pump and a fluidic flow was started. A fluidic flow rate of 40µl/min was applied for 6 days from day 7 to day 13 with a media change on day 10 for phase III (C) media. This flow rate was chosen as it coincides with that used on the kidney organoids, in which an effect on the vasculature was seen. It has been applied at this stage of differentiation, due to this being when branching occurs. On day 13, organoids were moved from the microfluidic device to a 96 well plate in 100µl of phase IV media.

Table 4. Phases of media needed for organoid generation

Media	Components
Phase I	STEMdiff APEL2, CHIR99021 (3μM), BMP4 (50ng/mL), VEGFA (50ng/mL), FGF2 (50ng/mL)
Phase II	STEMdiff APEL2, BMP4 (50ng/mL), VEGFA (50ng/mL), FGF2 (50ng/mL), hSCF (25ng/mL), Flt3 (25ng/mL)
Phase III (A)	STEMdiff APEL2, KO serum (5%), Heparin (5U/mL), VEGFA (100ng/mL), VEGFC (50ng/mL), FGF2 (50ng/mL), TPO (50ng/mL), EPO (50ng/mL), Flt3 (50ng/mL), hSCF (50ng/mL), BMP4 (50ng/mL), G-CSF (50ng/mL), IL3 (20ng/mL), IL6 (20ng/mL)
Phase III (B)	STEMdiff APEL2, KO serum (5%), Heparin (5U/mL), VEGFA (50ng/mL), VEGFC (25ng/mL), FGF2 (25ng/mL), TPO (25ng/mL), EPO (25ng/mL), Flt3 (25ng/mL), hSCF (25ng/mL), BMP4 (25ng/mL), G-CSF (25ng/mL), IL3 (10ng/mL), IL6 (10ng/mL)
Phase III (C)	STEMdiff APEL2, KO serum (2%), VEGFA (50ng/mL), VEGFC (25ng/mL), FGF2 (25ng/mL), TPO (25ng/mL), EPO (25ng/mL), Flt3 (25ng/mL), hSCF (25ng/mL), IL3 (10ng/mL), IL6 (10ng/mL)
Phase IV	StemPro-34, KO serum (2%), CD lipids (2%), VEGFA (25ng/mL), VEGFC ((25ng/mL), FGF2 ((25ng/mL), hSCF ((25ng/mL), Flt3 ((25ng/mL), TPO (10ng/mL), EPO (10ng/mL), IL-3 (10ng/mL), IL-6 (10ng/mL)

Imaging

Whole mount imaging

A minimum of six organoids were pooled together. Organoids were fixed with 4% paraformaldehyde (PFA) for 30 minutes on a rocker and washed with phosphate buffered-saline with 0.1% Tween (PBS-T). They were then placed in blocking and permeabilization buffer containing 2% goat serum, and 1%bovine serum albumin (BSA) in 1X PBS, 250μl

Triton X-100, 250µl Tween-20 and 500µl of 1% sodium deoxycholate, overnight on a roller. After blocking, primary antibodies were prepared in blocking buffer and incubated overnight at 4°C on a rocker. Organoids were washed 4 times with PBS-T, secondary antibodies and DAPI were prepared in PBS and added. Organoids were incubated overnight at 4°C on a rocker in the dark. Organoids were washed with 1mL PBS-T 4 times and were transferred into a glass bottomed imaging chamber. They were embedded in low melting point agarose and cleared. Organoids were cleared by dehydrating using a series of ethanol dilutions (30%, 50%, 70%, 90%, 100%) and then ethyl cinnamate was added. Alternatively, once embedded, organoids were cleared by adding acrylamide for an hour. They were imaged on the multiphoton LSM980 AiryScan Zeiss or LSM880 AiryScan Zeiss microscope. Antibodies and lectins used can be found in table 5.

Table 5. List of primary and secondary antibodies, lectins and dyes used in immunostaining of whole mount and cryosections and flow cytometry

Target	Host	Fluorophore	Catalogue No	Company	Dilution
		Primary antibodies			
Anti-CD34	Mouse	Unconjugated	343502	Biolegend	1:200
Anti-CD34	Rat	Unconjugated	sc-18917	Santa Cruz	1:200
Anti-VE-Cadherin	Mouse	Unconjugated	Sc-9989	Santa Cruz	1:200
Anti-CD19	Rabbit	Unconjugated	Ab134114	Abcam	1:100
UEA-1	Gorse Bush	UEA-1	GTX01512	GeneTex	1:100
		Secondary antibodies			
Anti Rabbit IgG	Goat	Alexa 488	A-11008	Invitrogen	1:300

Anti Rabbit IgG	Goat	Alexa 647	A-21244	Thermo Fisher	1:300
Anti Mouse IgG	Goat	Alexa 514	A-31555	Thermo Fisher	1:300
Anti Mouse IgG	Goat	Alexa 568	A-11004	Thermo Fisher	1:300
Anti Rat IgG	Goat	Alexa 647	A-21247	Invitrogen	1:300
DAPI	-	Uncongugated	D9542-1MG	Sigma-Aldrich	1:15000
Annexin V	-	PE	640947	Thermo Fisher	1:200
Anti-CD31	-	APC-Cy7	303120	Proteintech	1:200

Cryosectioning

A minimum of six organoids were pooled together per cryoblock. Organoids were fixed in 4% PFA for 30 minutes. They were transferred into a cryomold, and PBS was removed. A thin layer of OCT was added, and snap froze in an ethanol-dry ice bath. Once completely frozen, a second layer of OCT was added and snap frozen. OCT blocks were stored at -80°C. Using a cryostat, the OCT blocks were sectioned at 12 µm and placed on Superfrost adhesion microscope slides. Slides were stored in -80°C until stained.

Immunostaining

OCT sections were drawn around using a hydrophobic pen and blocking/permeabilization buffer was added for 1 hour at room temperature. After blocking, primary antibodies were prepared in blocking buffer and added for 2-3 hours at room temperature in a humid chamber. Sections were washed 3 times with PBS. Secondary antibodies and DAPI were prepared in PBS and added for 1 hour in a humid chamber. Sections were washed and a coverslip with ProLong Gold was added. Slides

were now ready to image using the LSM880 AiryScan Zeiss or LSM980 Upright Zeiss confocal microscope. All antibodies used are listed in Table 5.

Angiotool analysis

Whole mount images were processed so they all displayed the same depth images using a python code (Appendix 1). Pre-processing of the whole mount image was performed on ImageJ, including adjusting brightness and contrast, splitting the channels to focus solely on the vasculature, performing max intensity projections on the Z stacks and subtracting background to get the clearest image of the vessels. The processed max intensity image was then put into the angiotool plugin where the parameters (Figure 2), such as vessel length and intensity, were adjusted to create an overlay that was representative of the vessels within the organoid. The overlay and quantified output were saved as a JPEG image and excel sheet respectively.

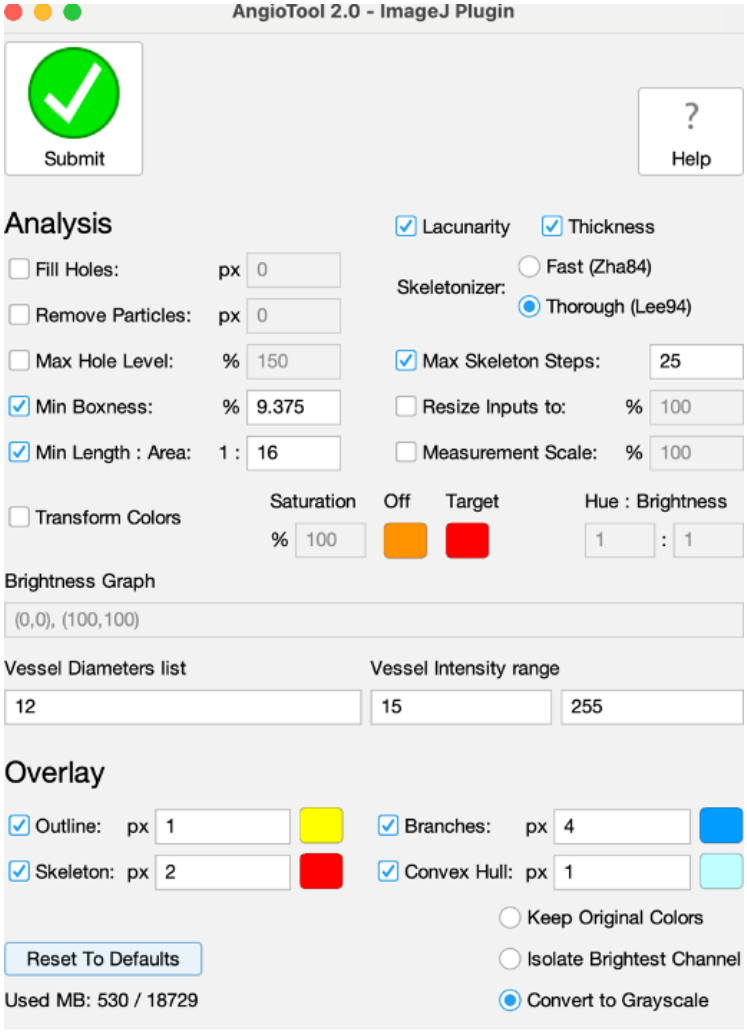


Figure 2. Angiotool ImageJ plugin default parameter settings

Flow cytometry

Organoid dissociation

Dissociation buffer was prepared on ice that contained Collagenase D at 2mg/mL, 1000U/mL DNase and 1% FBS in PBS. Organoids were transferred into a 15mL falcon tube and centrifuged at 400g for 4 minutes. The media was removed, and organoid pellet washed with 10mL of PBS three times. 1mL of collagenase D was added for every 20 organoids and placed in the shaking incubator for 1 hour. Using a P1000 and P100 positive displacement pipette, the organoids were triturated vigorously until a single cell suspension was formed. Dissociation buffer was added to stop digestion. Viability was

checked using trypan blue and the single cell suspension was either used for flow cytometry immediately or frozen and stored in liquid nitrogen.

Cell viability and apoptosis assay

Dissociated organoids were placed in a V-bottom 96 well plate and centrifuged. Media was aspirated and resuspended in 100µl of annexin buffer containing annexin V at 1:200 dilution for 20 minutes. DAPI was added to annexin buffer at 1:7500 in 100µl. This was added to the samples to create a final volume of 200µl with DAPI at 1:15000. Stained cells were analysed on the CytoFLEX S and CytoFLEX 355. Analysis and gating were performed on FlowJo. Flow dyes used are listed in Table 5.

Endothelial cell count

Dissociated organoids were placed into a V-bottomed 96 well plate and centrifuged. Media was aspirated and resuspended in 50µl of PBS 5% FBS containing CD31 at 1:200 dilution. They were stained for 20 minutes on ice. Stain was removed and 100µl of annexin buffer containing annexin V was added for 20 minutes. DAPI was added at 1:15000 in annexin buffer to make a final volume of 200µl. Stained cells were analysed on the CytoFLEX S and CytoFLEX 355. Analysis and gating were performed on FlowJo. Flow dyes used are listed in Table 5.

Cloning

Primer design

Hou et al described the VE-Cadherin promoter region as 1124bps between -1031bp and +93bp which relates to the first base pair of their reported VE-cadherin cDNA. He also used mutant promoter regions that were smaller including -341/93bp (Hou et al., 2021). Using the eukaryotic promoter database, the whole sequence for VE-cadherin/CDH5 gene was used to extract the regions of interest (-1031/93 and -341/93bp). These sequences were then placed into PrimerBlast, with a reverse primer being designed based on the last 20bps of the promoter sequence. PrimerBlast outputted multiple forward primer sequences that were picked based on off target

products and GC content. The selected primers were then placed into NEbuilder to add overhangs, in order to assist with joining of plasmid fragments. Additionally, using a pMC-PDGFRB-lifeact-miRFP-P2A-mito-mOrange plasmid designed by the Fielding Lab, primers for the backbone fragment (excludes PDGFRB and mOrange regions) and miRFP fragment were designed (Fig 3). All primer sequences are found in table 6.

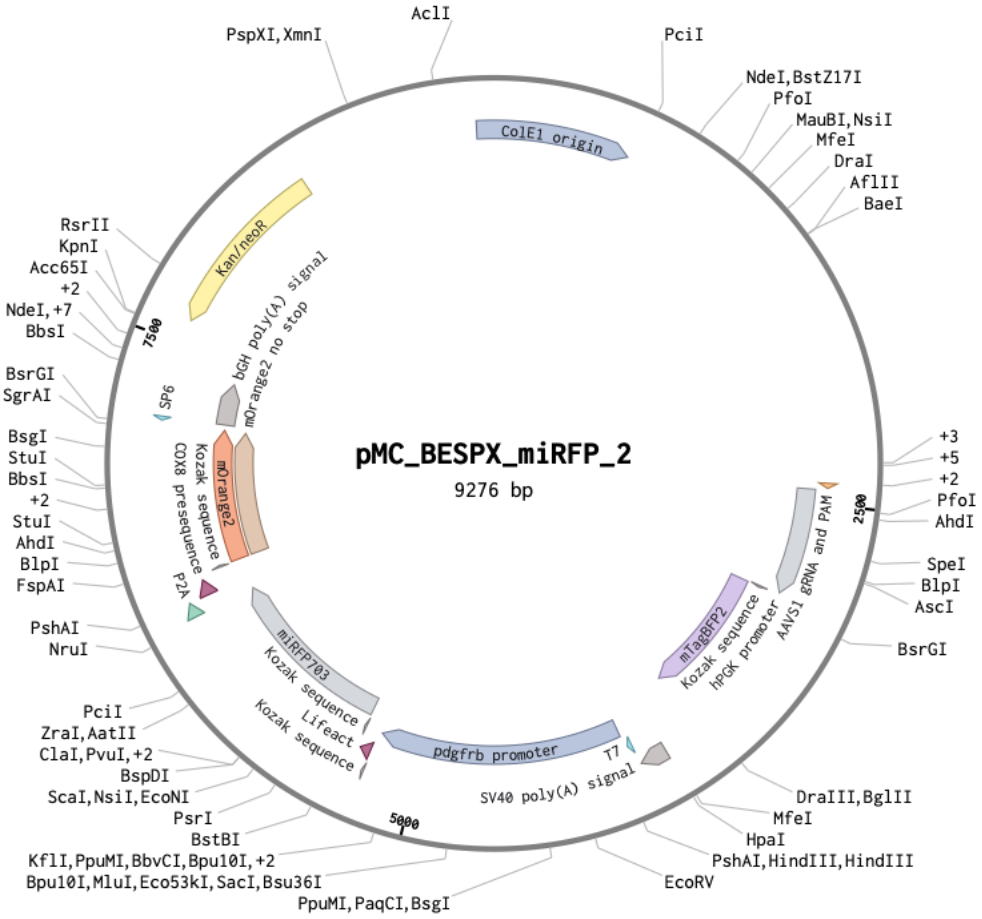


Figure 3. Plasmid sequencing used for primer design.

Designed on benchling by Juma Ward in Fielding Lab at University of York

Table 6. Primer sequences for plasmid design

FWD, Forward, REV, Reverse, lowercase letters are overhangs

Oligo Name	Sequence (5' to 3')
VE-Cadherin 1 FWD	CCTGGTCAGCAGAATCTTGGC
VE-Cadherin 2 FWD	GGAAACCATCCCAGGGGGAA
VE-Cadherin REV	AGGGGAGTGTGGGAGCCC

VE-Cadherin Promoter 1 FWD	cacatttgatCCTGGTCAGCAGAATCTTGGC
VE-Cadherin Promoter 2 FWD	cacatttgatGGAAACCATCCCAGGGGG
VE-Cadherin Promoter REV	ccatggtggcAGGGGAGTGTGGGAGCCC
Plasmid Backbone FWD	tgagagctaaCTATAGTGTCACCTAAATCTG
Plasmid Backbone promoter 1 REV	gctgaccaggATCAAATGTGGCCCTATAG
Plasmid Backbone promoter 2 REV	gatggtttccATCAAATGTGGCCCTATAG
miRFP FWD	acactcccctGCCACCATGGTAGCAGGTC
miRFP REV	gacactatagTTAGCTCTCAAGCGCGGTG

PCR

gDNA was isolated from human cells. Primers were reconstituted in nuclease-free water to a concentration of 100mM and a working 10µM stock was made. Following the NEBuilder Q5 High-Fidelity DNA polymerase protocol, a master mix containing Q5 reaction buffer, Q5 DNA polymerase, dNTPs, nuclease-free water and DNA/plasmid template. The master mix is added to PCR tubes along with the corresponding forward and reverse primers. A PCR was run using a touchdown step to create higher specificity of the intended product, ensuring to use the correct annealing temperature. A 1% agarose gel was made by adding 0.4g agarose to 40mL 1xTAE and microwaving until fully dissolved. The gel was poured into the appropriate mould with appropriate comb and allowed to cool. The gel was placed into an electrophoresis tank and covered with 0.25xTAE until all wells are covered. 5µl of PCR product was mixed with 1µl of tri-track and carefully loaded into the wells. The appropriate ladder was placed into the gel either side of the PCR product. Gel was run at 300V for 10 minutes and visualised using a UV transilluminator.

Results

Optimising vessel staining

In order to determine the structure of the vasculature generated within the bone marrow organoids, both whole mount imaging and cryosection analysis was performed. Several markers were evaluated and compared for their ability to delineate the vasculature.

Whole mount imaging

Initially, organoids were stained with the lectin UEA-1, which binds to the alpha-L-fructose (Fig 4A). This stain was associated with a high level of background autofluorescence, which made it difficult to analyse the vessels. The UEA-1 marker seemed to bind to the collagen in which the organoids were embedded during culture. Washes between primary and secondary staining were increased from 3 to 5, and PBS-T was used rather than just PBS, but this seemed to have no improvement. Additionally, UEA-1 was unreliable, only working twice out of many attempts.

Next, the pan-vessel marker VE-cadherin was evaluated as a vascular stain. As seen in Fig 4B, anti-VE-cadherin staining generated a much clearer display of the vasculature within the organoid (Fig 4B).

CD34, which is a marker of developing vessels, was also evaluated. Initially, staining with an antibody against CD34 did not result in any visible images in the whole mount process. Upon another attempt, anti-CD34 did bind to the vasculature (Fig 4C). In further imaging, I went forward with the use of anti-VE-cadherin due to the production of less background fluorescence compared to UEA-1 and anti-CD34 in the same organoid, resulting in easier analysis of the vasculature.

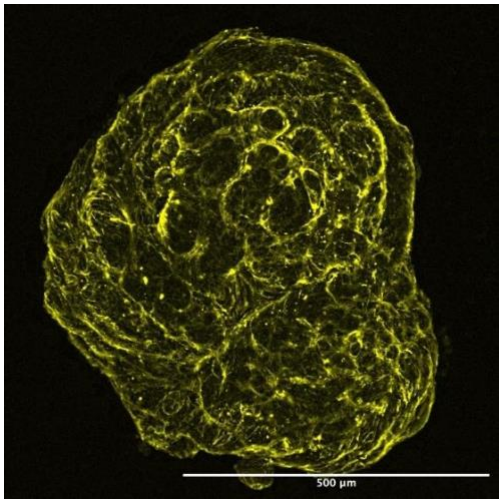
DAPI was used as a nuclear stain but seemed to bind to streaks of dust or plastic within the sample (Fig 4D). This made it difficult to image DAPI in the organoid. However, it was important to include DAPI in the imaging process to separate individual organoids. Moving forwards the interpretation of DAPI staining was done with caution.

Cryosections

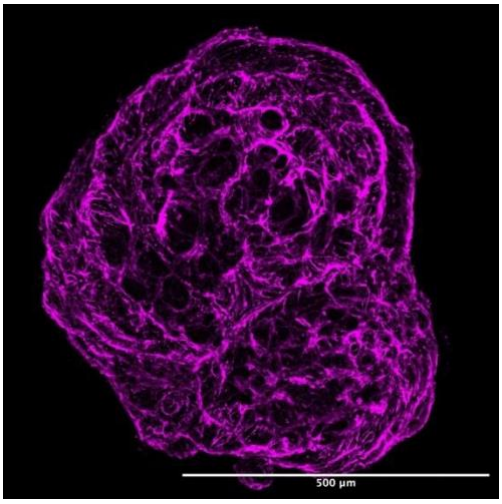
Anti-VE-cadherin (Fig 4E) and anti-CD34 (Fig 4F) antibodies were also evaluated as vasculature stains in cryosection imaging. All cryosections were cut into 12µm slices for analysis. Both stains were found to be satisfactory for use in cryosections, but for consistency between the cryosections and whole mount, VE-cadherin was used as the primary vessel marker for further analysis.

Whole Mount Images

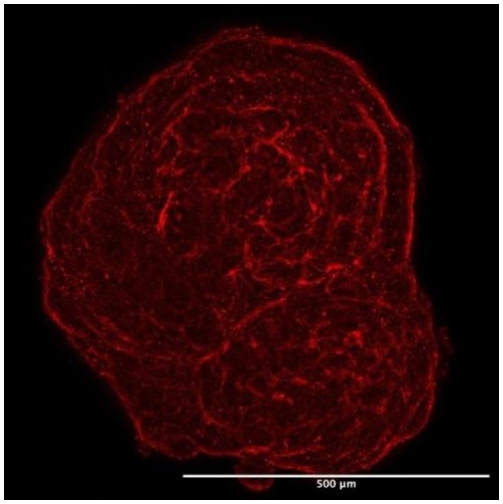
A



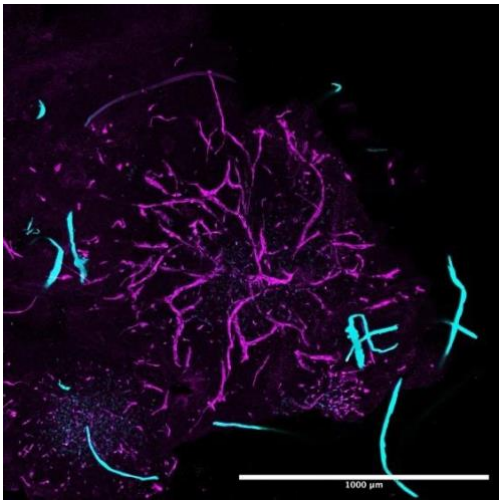
B



C

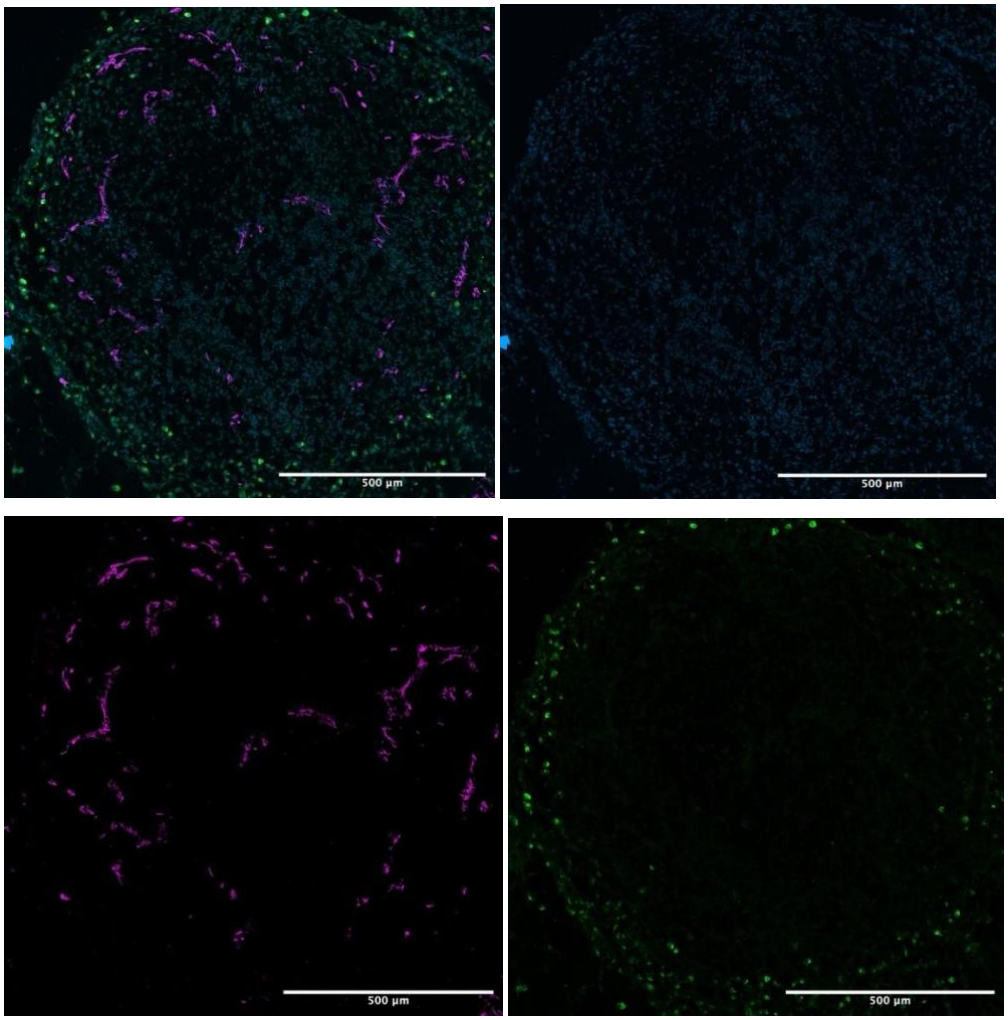


D

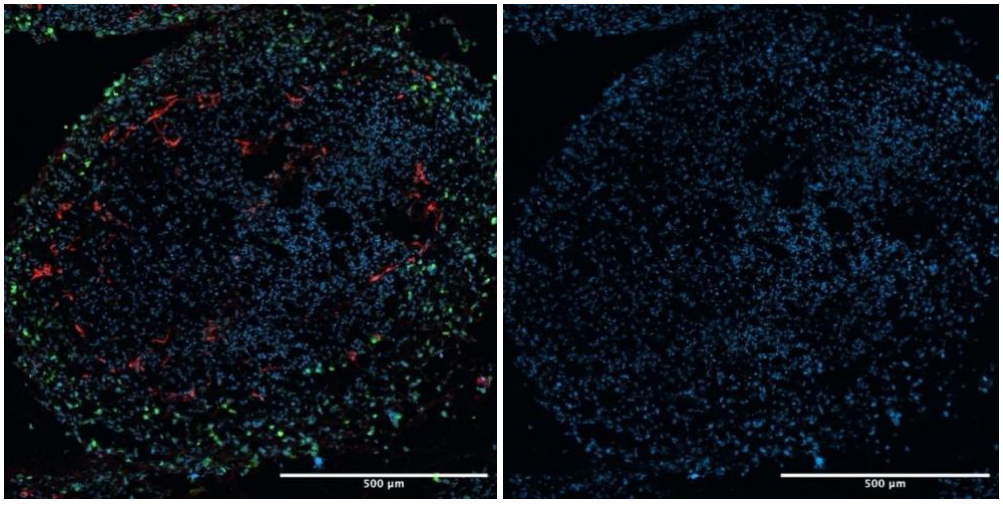


Cryosections

E



F



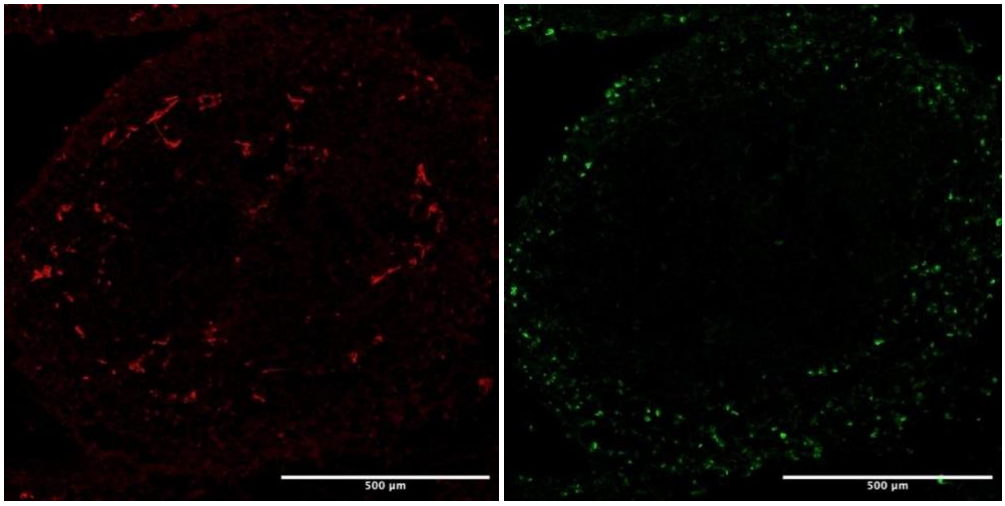


Figure 4. Optimisation of antibody staining.

(A-C) Max intensity projection of whole mount imaging of a control organoids vasculature stained with (A) UEA-1, yellow (B) anti-VE-cadherin, magenta (C) anti-CD34, red. (D) Max intensity of whole mount imaging of control organoid stained with anti-VE-cadherin (magenta) and DAPI (blue). (E) Max intensity of 12µm cryosection slice of control organoid stained with DAPI (blue), anti-VE-cadherin (magenta) and anti-CD19 (Green). (F) Max intensity of 12µm cryosection slice of control organoid stained with DAPI (blue), anti-CD34 (red) and anti-CD19 (Green). All concentrations of antibodies can be found in table 5.

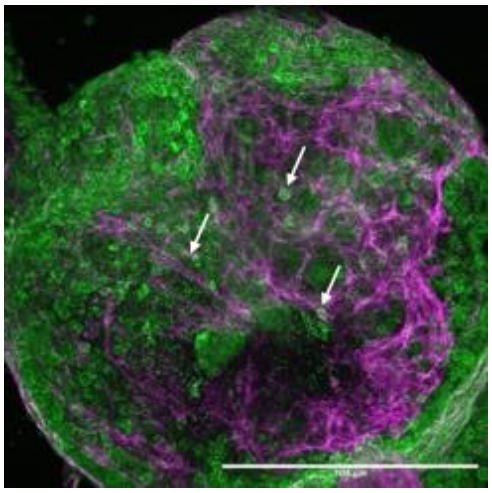
Baseline distribution of ALL cells within bone marrow organoids

The B-ALL cell lines SD-1 and SEM were used to analyse engraftment of B-ALL cells into the bone marrow organoid. On day 14, 6000 ALL cells per organoid were resuspended into the phase IV media for engraftment of the organoid. Whole mount imaging and cryosections were used to validate the engraftment of ALL cells into the organoids (Fig 5A and 5B). Staining of the B-ALL cells was done using anti-CD19 and/or CellTrace (Fig 5C). The B-ALL cells were stained with CellTrace before engraftment, because CellTrace is a proliferation dye, it will reduce in brightness as the cells divide. This explains why some B-ALL cells will be stained with anti-CD19 and not CellTrace.

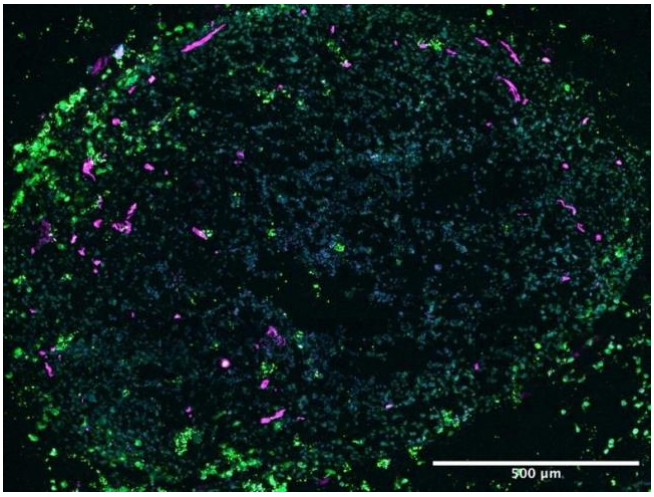
The ALL cells seemed not to be able to penetrate the centre of the tissue and instead engraft around the outside of the organoid. Figure 5A displays max intensity imaging that indicates B-ALL engraftment in the centre of the organoid, which suggested greater B-ALL

penetration into the organoid. However, when looking at each Z-stack individually, it becomes apparent that engraftment is still restricted to the edge of the organoid. Z-Stack 3, which indicated roughly 9µm depth into the organoid, (Fig 5D) displayed ALL cells centrally, compared to Z-stack 26, roughly 78µm into the organoid, that only showed engraftment around the edge. This pattern continues as we imaged deeper into the organoid (Fig 5F). This creates an illusion of greater penetration and engraftment of ALL cells.

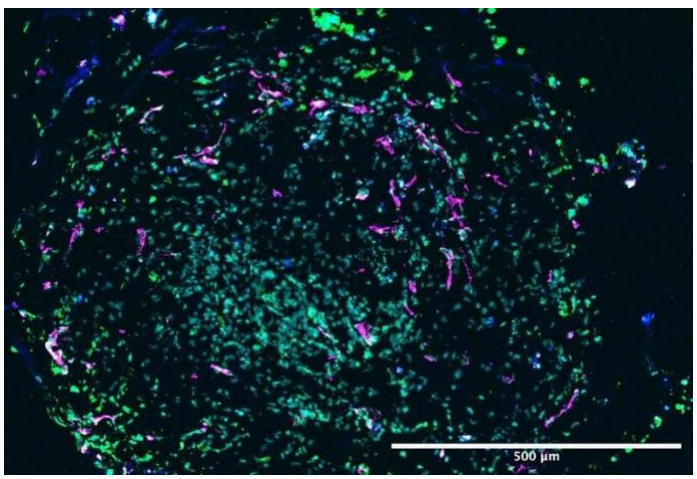
A



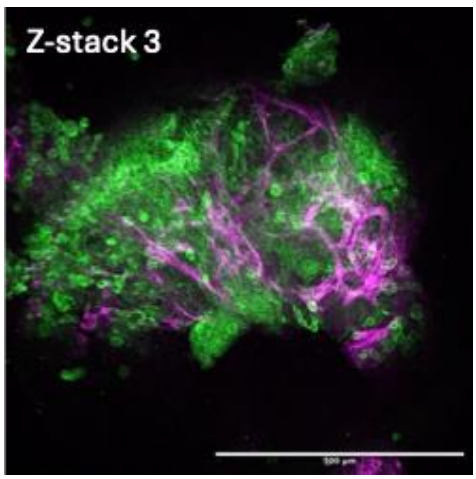
B



C



D



E F

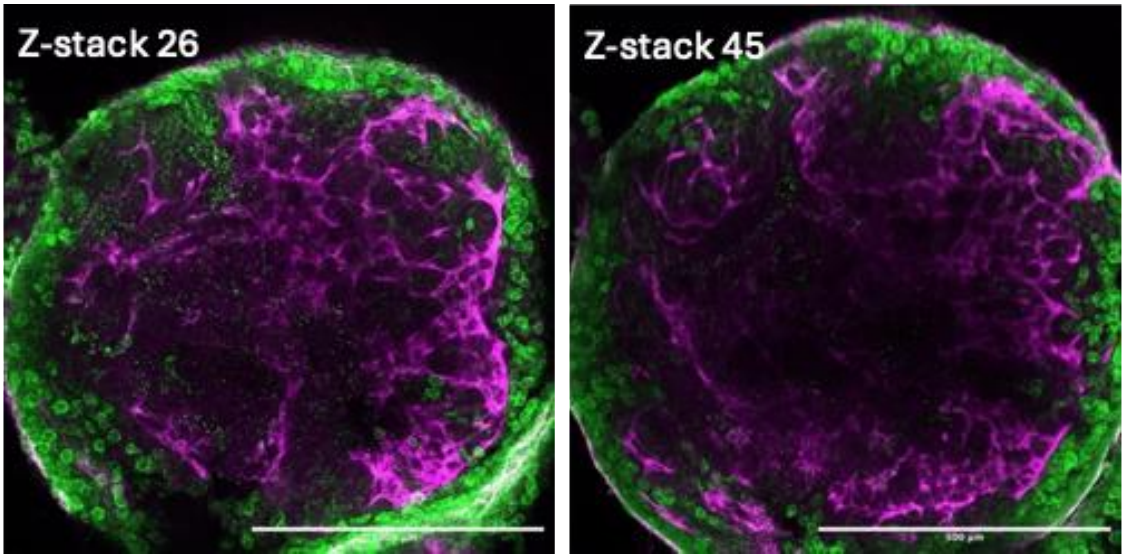


Figure 5. Engraftment of ALL cells in organoids.

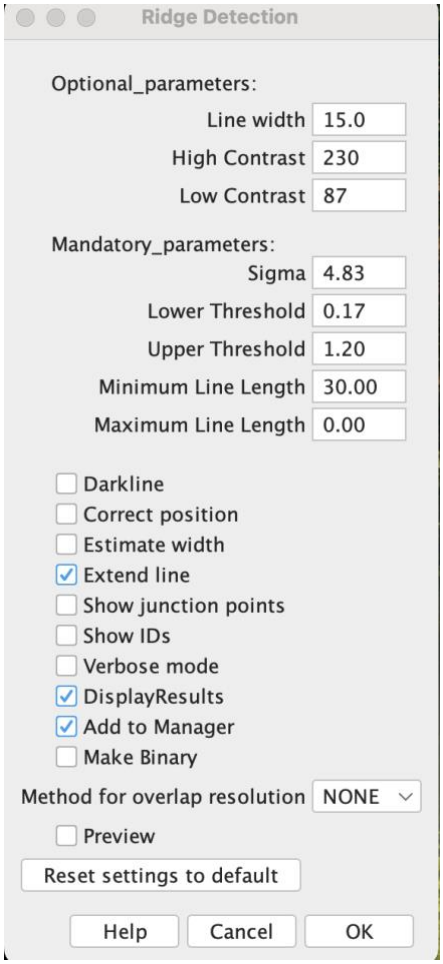
(A) Max intensity of whole mount imaging of ALL engraftment in control organoid stained with anti-VE-cadherin (magenta) and anti-CD19 (green), CD19 positive cells appear to be evenly distributed through the centre of the organoid (White arrows). (B) max intensity of 12µm cryosection of control organoid stained with DAPI (blue), anti-VE-cadherin (magenta) and anti-CD19 (green). (C) max intensity of 12µm cryosection of control organoid stained with DAPI (cyan), anti-VE-cadherin (magenta), anti-CD19 (green) and CellTrace (Blue). (D-F) Different Z stacks of whole mount imaging in Fig 4A to display difference in engraftment through organoid. Whole mount image was 153µm depth split into 50 Z-stacks. Stained with anti-VE-cadherin (magenta) and anti-CD19 (green). (D) Z-stack 3. (E) Z-stack 26. (F) Z-stack 45

Analysis of vasculature in organoids

During this experiment, the organoids were treated with cytarabine (AraC), which is a commonly used chemotherapy drug to treat B-ALL. Patients treated with AraC have been shown to develop vascular injury, causing direct necrotic effect on endothelial cells (Ahmed et al., 1998). Due to this I hypothesised that AraC would have an effect on the vasculature within the organoids, reducing the number of vessels due to apoptosis of

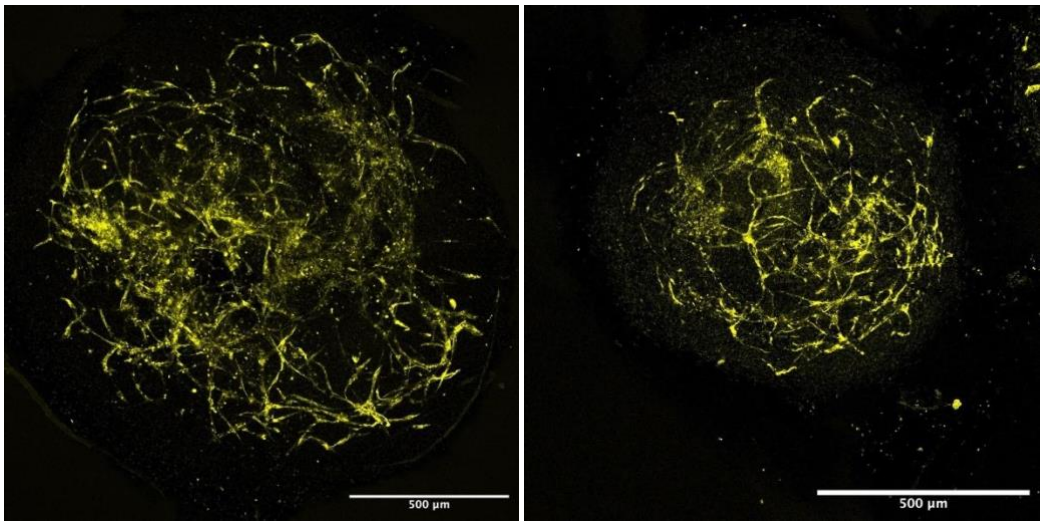
endothelial cells, therefore allowing this drug to be used to validate changes in the vasculature could be measured. The effect the addition of this drug had upon the vasculature was then analysed using different image analysis plugins to determine which was most effective moving forwards. Initially, an imageJ plugin called ridge detection was used. This analysis creates an overlay of the image using parameters such as line width and line length that can be adjusted (Fig 6A). Once parameters are set, the data output includes a list of the junction points and length of each vessel. For the context of the vessels, this would allow for the characterisation of the overall structure and organisation. Unfortunately, it produced unreliable results by incorrectly identifying vessels or missing parts of the vasculature (Fig 6B and 6C). Additionally, the quantitative outputs of ridge detection, included only junction coordinates and length of vessels that were not easily interpreted to produce conclusions. I identified angiotool, an imageJ plugin that produced an overlay of the vessels that can be easily adjusted using the parameters, including vessel diameter and pixel removal that ensures all vessels are included in the analysis, whilst small background is removed (Fig 6D).

A



B

Untreated AraC



C

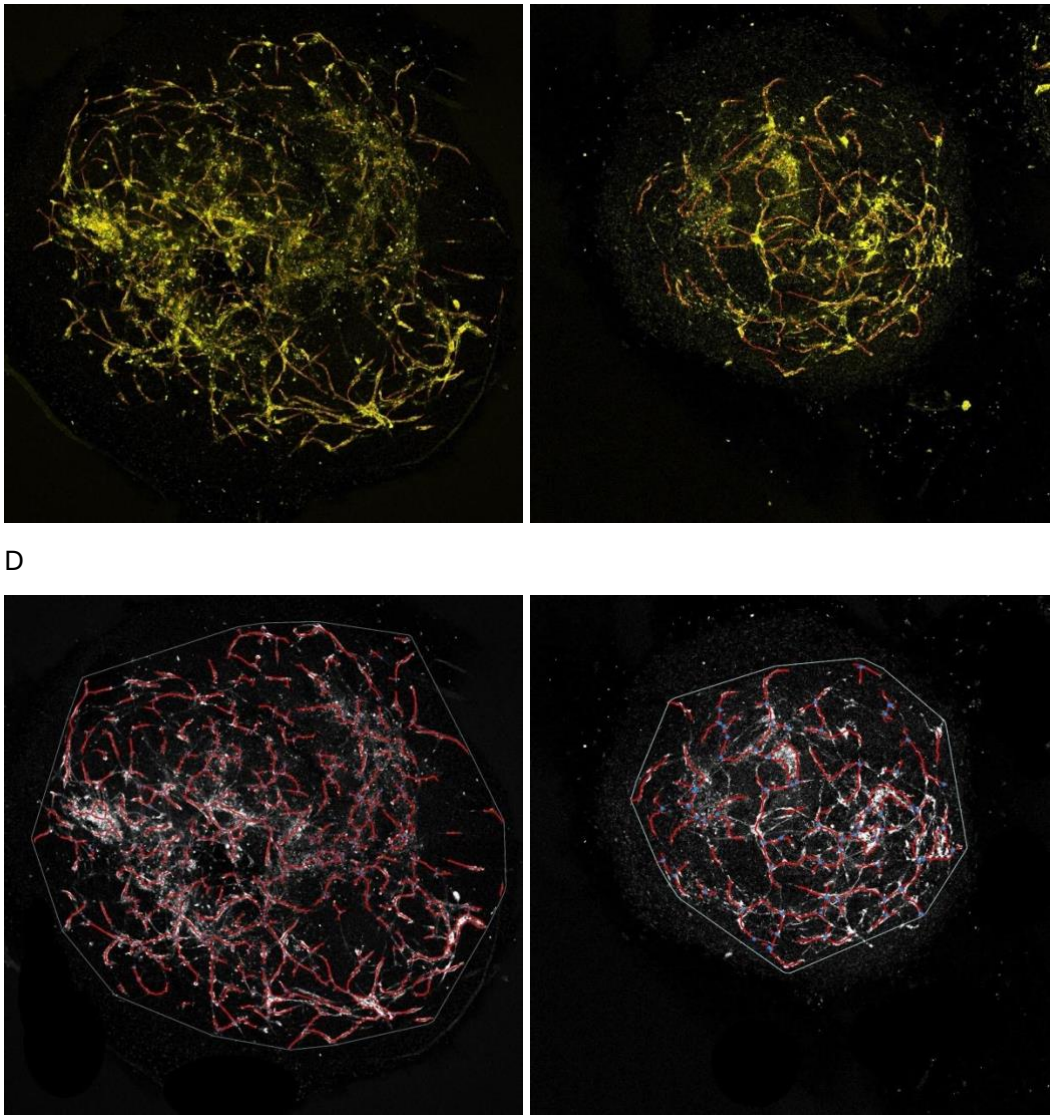


Figure 6. Vessel analysis methods.

(A) Parameter controls for ridge detection analysis. (B) max intensity projection of whole mount images of untreated organoid and organoid treated with 2μM of AraC stained with UEA-1 (yellow). (C) Ridge detection overlay (red) of max intensity whole mount image of untreated organoid and AraC treated organoid. (D) angiotool overlay of the vasculature of max intensity whole mount image of untreated and AraC treated organoid.

Evaluating angiotool: response of the bone marrow organoids vasculature to cytarabine treatment

I sought to quantify the effects that AraC had upon the vasculature within the organoid, with the expectation to see a decrease in all aspects. The organoids were either untreated or treated with 2μM of AraC for 48 hours. Preliminary analysis using the angiotool plugin displayed a trend towards an increase in the vessel percentage area in the organoids treated with AraC (Fig 7A). Additionally, the junction density increased, which is a sign of increased angiogenesis and branching (Fig 7B). The average vessel length is greater in the AraC treated compared to untreated, which could be a sign that AraC enhances the vasculature (Fig 7C). However, the AraC treated organoid is smaller in size, and this could be due to treatment with AraC or due to the variability between organoid generation in general. This data does suggest that the addition of AraC does impact the vasculature within the organoid. Importantly, this shows that the angiotool analysis provides more specific characteristics of the vessels that can be used together to get a more quantitative output on the effects different conditions have upon the vasculature. This experiment would need to be repeated to fully understand the effect of AraC on the vasculature in the organoids. Unfortunately, due to time limitations and staining troubles involving UEA-1 we could only obtain data for one organoid in each condition. Moving forward VE-Cadherin was used for all vasculature staining.

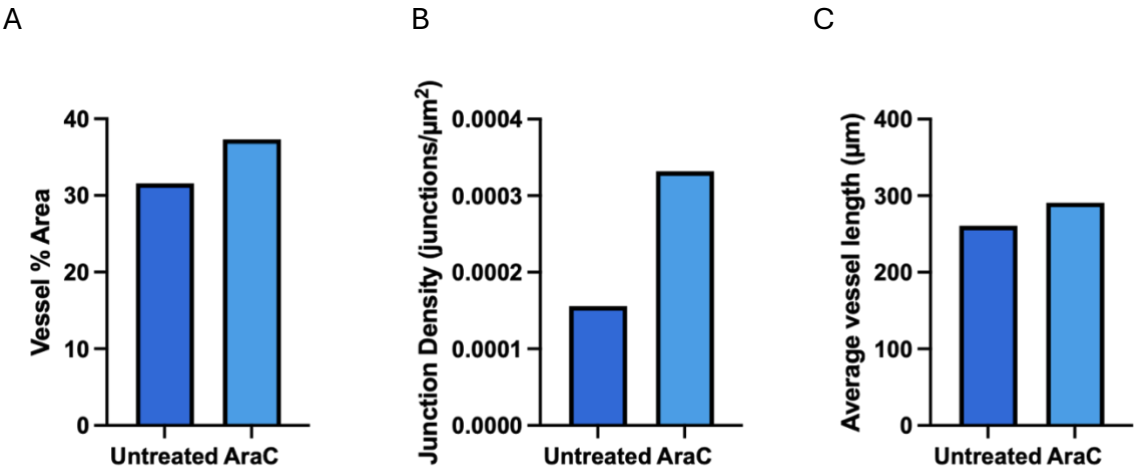


Figure 7. Treatment with AraC influences the vasculature within bone marrow organoids.

Angiotool analysis performed of whole mount images in Fig 5A, N=1. (A) Vessel percentage area of untreated compared to 2μM AraC treated organoid. (B) Junction density of untreated compared to AraC treated measured in junctions per μm^2. (C) average vessel length measured in μm.

Optimising dissociation of organoids flow cytometry analysis

Flow cytometry analysis is an important technique in determining the viability and cell types of the organoids generated. Dissociation of organoids creates a single cell suspension that was used to analyse the viability and cell types within the bone marrow organoids. The dissociation method described in Olijnik *et al*, incubated the organoids in collagenase D for 5 minutes, triturated vigorously and repeated until a single cell suspension was formed. This process took 40-60 minutes, and viability was determined using DAPI for late apoptosis and annexin for early apoptosis. This produced a viability of 72% but seemed to lose a lot of cells in the process, even with the use of positive displacement pipettes. We tested alternative methods to determine a more effective way of dissociation. Using a filter, vortex, cutting organoids with scissors and placing in a shaking incubator rather than trituration. All methods roughly took an hour to dissociate the organoids, but some were more effective than others. Filtering reduced the viability, whilst using a vortex was least effective at creating a single cell suspension. Overall, the most effective method was placing the organoids in the shaking incubator for an hour and triturating with P1000 and P200 pipettes, which had a viability of 89% and was the simplest method to perform (Fig 8).

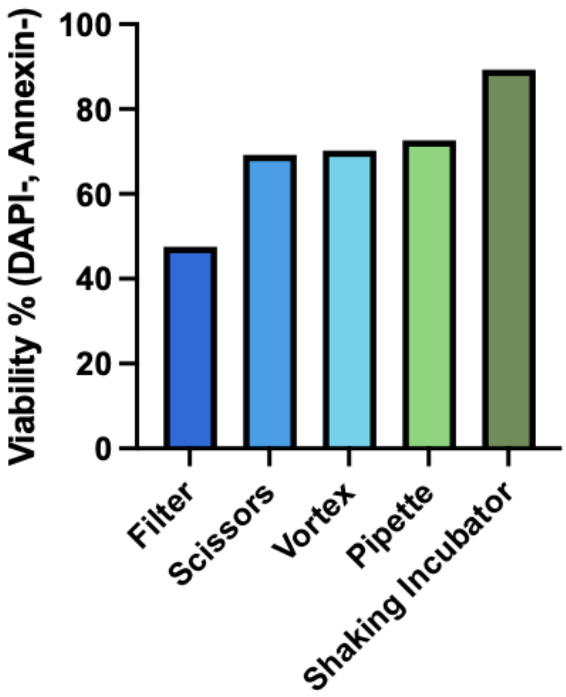


Figure 8. Viability of organoids is highest using shaking incubator for dissociation.

N=1, 7 organoids were pooled together in each condition: Filter, Scissors, Vortex, triturating pipette and shaking incubator.

Design of microfluidic chip and system

Optimising chip design

A microfluidic chip was designed to enable a laminar fluidic flow over the bone marrow organoids based on the work of Homan *et al*, who applied a fluidic flow to kidney organoids (Homan et al., 2019). In collaboration with the engineering department at the University of York, a 3D CAD model was designed by Dr Callum Silver and used to create a resin negative mould, in which PDMS was then inserted into and cured to generate an autoclavable microfluidic device. The design originally contained 30 U-bottomed microwells of 5x5x5mm, so the organoids could be individually embedded into hydrogel. This size was chosen to allow for enough hydrogel for effective vasculogenesis over the 10 days of culture. Initially, there was a gap of 2mm above the microwells to allow for the inlet and outlet tubing to connect to the device (Fig 9A). To seal the device and create a closed system, a 3D printed casing was designed. The initial casing only allowed for

visualisation of the organoids and flow of the system from beneath, which made it difficult to see the development of the organoids under flow (Fig 9B). The casing was adjusted to be identical on both sides for better visualisation of the organoids throughout culture (Fig 9C).

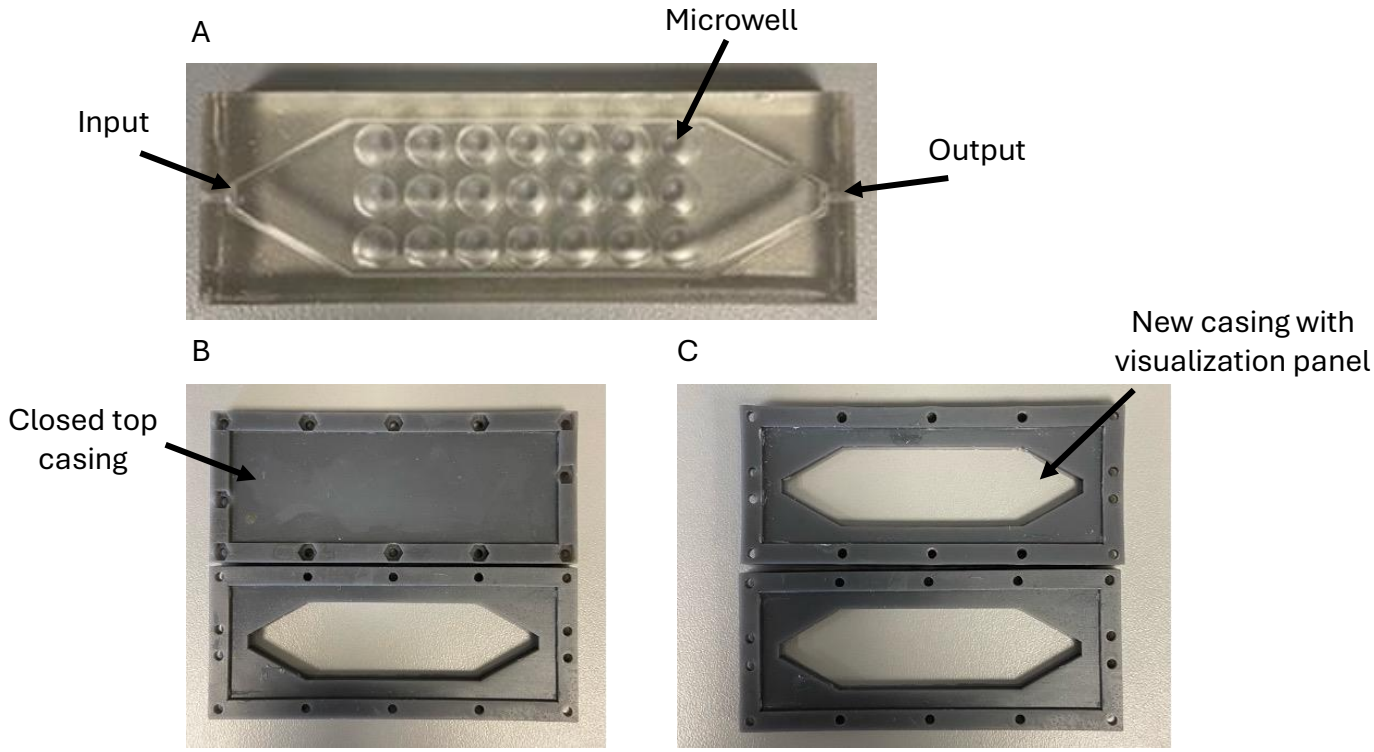


Figure 9. Initial chip design and casing evolution.

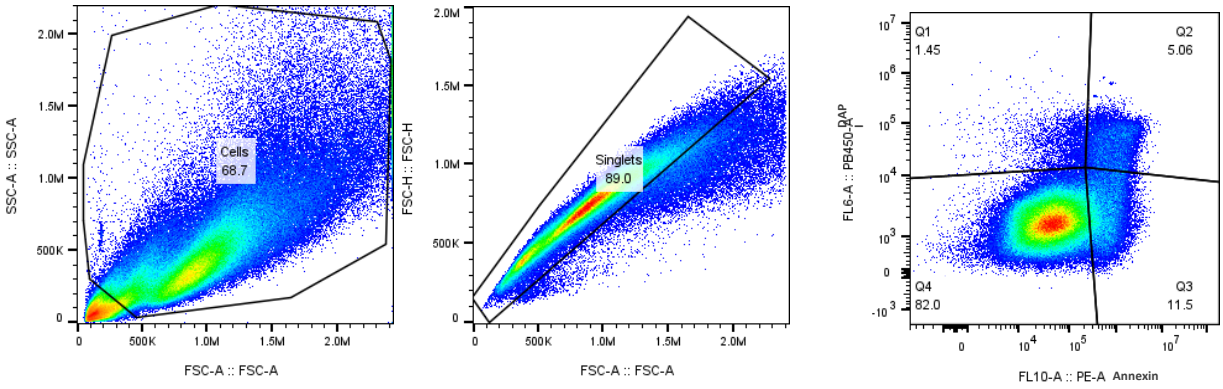
(A) Initial microfluidic chip with 21 microwells of 5x5x5mm and a 2mm channel above the microwells. (B) Initial casing design of microfluidic chip with top being enclosed with a slide and bottoming including hole to visualise organoids that are screwed together to create a seal and closed system. (C) New design for casing of microfluidic design that allows for improved visualisation.

During the initial run of the microfluidic chip, multiple issues were discovered. These included how to embed the aggregates into the microwells and the major problem of the production of bubbles in the system. These bubbles restricted the fluidic flow and

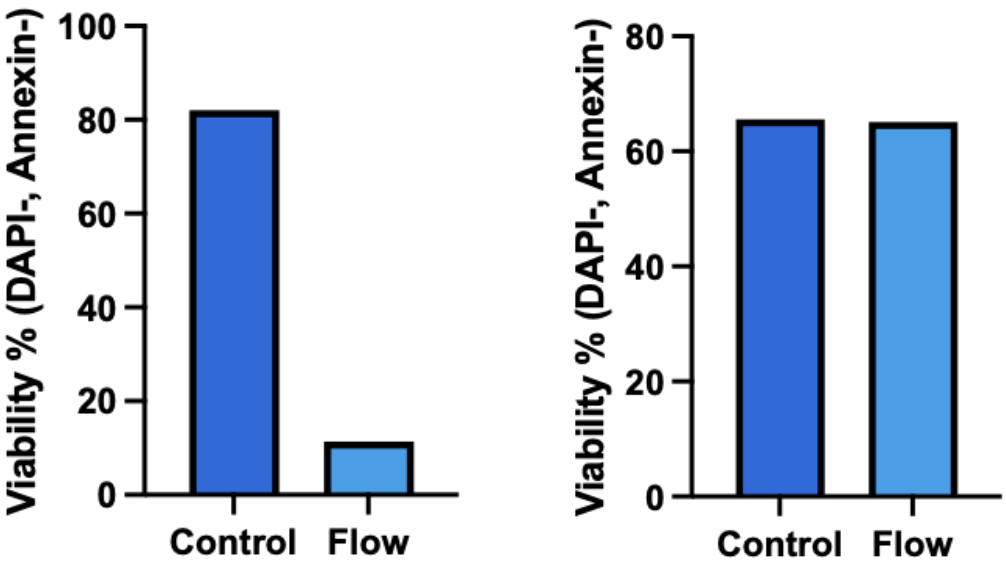
generated air pockets over the microwells and around sharp corners of the device that were not pushed through the system. This led to a concern of limited access of media for the organoids. Due to this, the viability of the organoids under this condition was determined using flow cytometry. The addition of flow using the initial design resulted in a viability of 11% compared to the control organoid of 82% viability (Fig 10A and 10B).

To address the issue of bubbles, I reduced the size of the microwells to 25µl. This size was chosen, to allow for enough hydrogel to promote vascular sprouting whilst reducing the space for air bubbles to become trapped within the microwells. Additionally, to create a more uniform flow over the organoids, the channel above the microwell was reduced to 1mm. This re-design required a readjustment of how the inlet and outlet tubing were positioned, due to the channel being smaller than the diameter of the rigid tubing. Bubbles were still being produced in this new design, but they were now being pushed over the organoids and through the system. Additionally, this new design increased the viability of the flow organoids to 65%, which was the same as in the control condition (Fig 10C). As well as increasing the viability by 50% between the two design attempts, the apoptotic population also decreased (Fig 10D).

A



B C



D

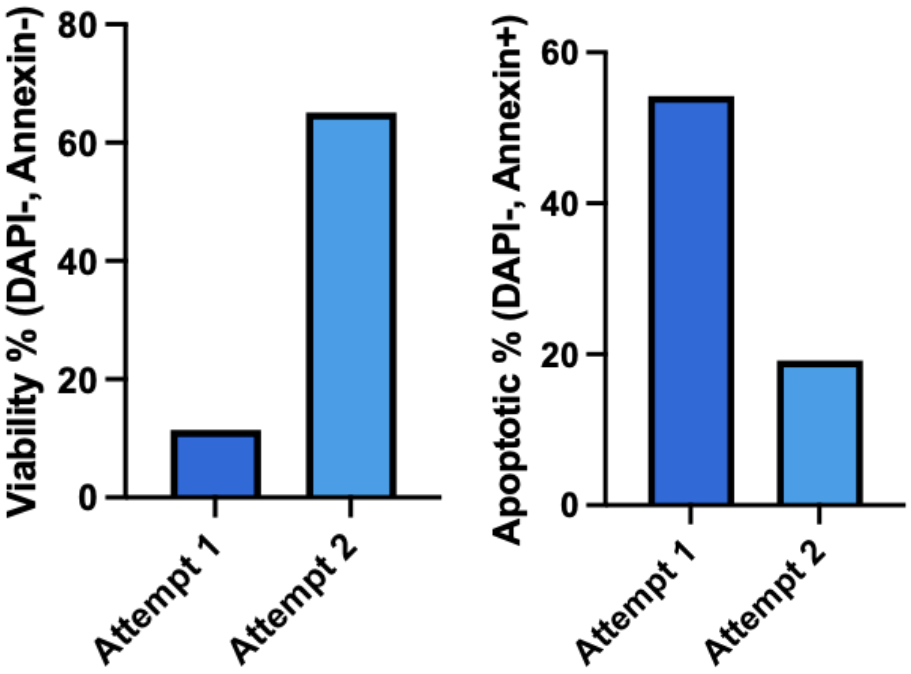


Figure 10. Flow-cytometric determination of the viability of fluidic flow organoids increased with new microfluidic chip design.

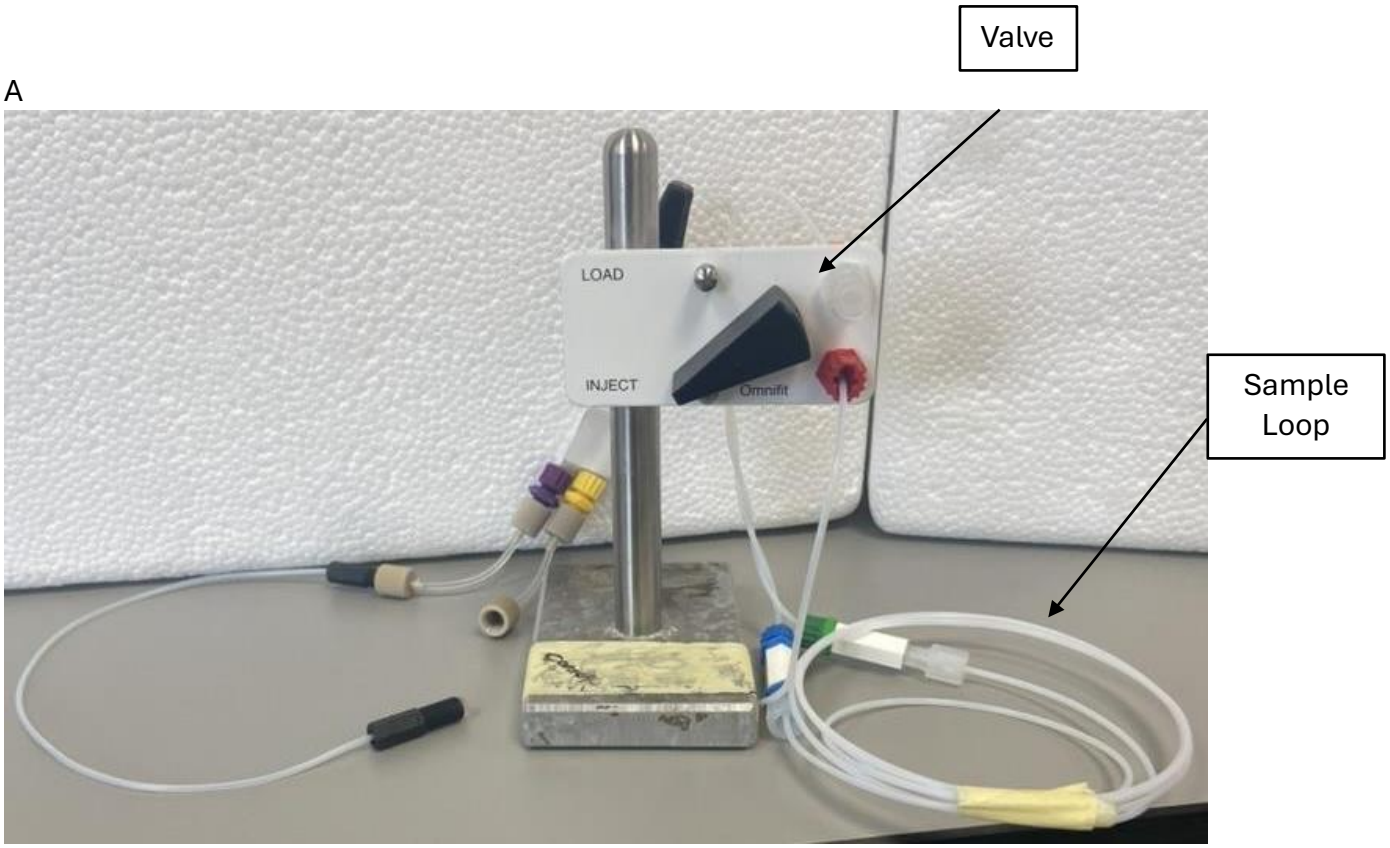
(A) Gating strategy for cells, singlets and DAPI (PB450) vs Annexin (PE) for viability. (B) Viability of control and flow organoid of initial microfluidic chip design. (C) Viability of control and flow organoid of second design. (D) viability and apoptotic percentage of attempt 1; with initial microfluidic chip design vs attempt 2; microfluidic chip with reduced microwells (25µl) and reduced channel space (1mm). N=1

Optimising fluidic system

To generate flow over the organoids the microfluidic chip was connected to 1/16 inch inner diameter (ID) rigid tubing, that was in turn connected to 1mm ID peristaltic tubing using PEEK male and female connectors. All tubing and connectors were flushed with ethanol and autoclaved before use to ensure a sterile environment. With the goal to achieve constant and uniform flow over the organoids, a sample loop was added to the system (Fig 11A). A sample loop is an extra loop of tubing that was added into the system and using a valve could be disconnected when needed. The aim of this was to apply sufficient flow to push all bubbles within the system into the sample loop tubing and disconnect this tubing from the whole system. Unfortunately, the valve which disconnects the tubing from the system was not autoclavable, so the small amount of tubing was sterilised using ethanol. This approach was unsuccessful as it resulted in a bacterial infection. Due to this tubing being within the sample loop valve it could not be sterilised by UV irradiation, this resulted in the sample loop being removed to avoid further risk of infections.

As an alternative to the sample loop, an autoclavable bubble trap was added to the system (Fig 11B). It was connected to rigid tubing and placed before the microfluidic chip to trap the bubbles before they reached the organoids in the microfluidic chip. The viability of the organoids was evaluated after these modifications and no improvement was seen in the viability, but the apoptotic population did decrease (Fig 11C).

A



B



C

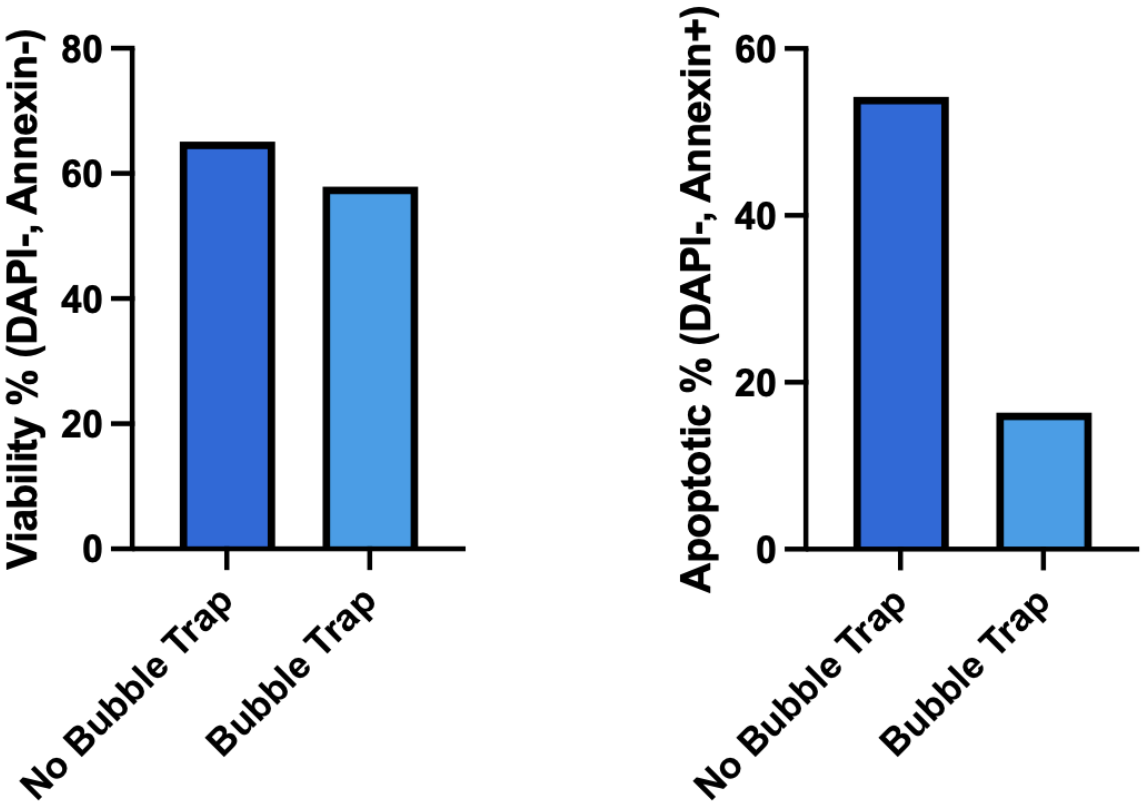


Figure 11. Addition of a bubble trap does not improve the viability of bone marrow organoids.

(A) Labelled sample loop and valve. When valve is turned to inject, sample loop is connected to the system and can be filled. When turned to load the sample loop is disconnected from the system. (B) Bubble trap that is connected to system using female PEEK connectors. (C) Viability and apoptotic percentage of organoid in system with no bubble trap and bubble trap included N=1.

Elimination of bubbles

The production of bubbles within the microfluidic system was a problem throughout all designs (Fig 12A and 12B). It not only impacted the viability of the organoids but the fluidic flow as well. I performed optimisation experiments, adjusted microfluidic design and system design to try eliminating bubbles from within the system. There were many

possible reasons that could produce bubbles and approaches that were considered or were taken to eliminate them are listed in Table 7.

Table 7. Approaches to eliminate bubbles from microfluidic system

Approach	Summary	Outcome
Clamp	A clamp was applied to peristaltic tubing once system had been primed with media due to media being forced out of tubing whilst creating a closed system	Approach continued – small or no air bubble within the initial system before flow was applied
Degas media	The media used for culturing the organoids has dissolved gases within it that can create bubbles, degassing the media would remove all dissolved gases through applying heat and vacuum	Approach disregarded – Degassing the media is a difficult procedure that required specific equipment that was not available. Additionally, media would have needed to be sterilised after making this a long process for each different phase of media
PDMS	PDMS is a commonly used material in microfluidics for its highly advantageous characteristic of gas permeability and transparency, but this property also means it can absorb small molecules and allows water vapours to diffuse through it (Toepke and Beebe, 2006)	Approach continued – PDMS was used as this is the main material used in microfluidics and was recommended by the engineering department who had lots of experience in this area
Sample loop (Fig 11A)	A sample loop is an extra loop of tubing that is attached to the fluidic system that can be disconnected using a valve. This would allow for	Approach disregarded – sample loop contained small amount of tubing within valve that could not be sterilised by autoclave and/or

	bubbles to become trapped in the additional loop and then disconnected from the system	UV radiation. Attempts of sterilisation by ethanol were unsuccessful and an infection occurred upon use.
Bubble trap (Fig 11B)	A bubble trap has a hydrophobic membrane that when a liquid flows through bubbles are expelled but no liquid is lost	Approach continued – This device was autoclavable so easily sterilised for use and could be added simply to the system, creating a more uniform flow over the organoids with a reduction of bubbles within the system
Filling microwells	Bubbles within the system were getting trapped above microwells in new design (Fig 12C). Upon consultation with the engineering department, it was suggested that incomplete filling of the microwells would leave room for air to be trapped above the wells	Approach continued – Experiment were microwells were filled with completely with 25µl of agarose showed no bubbles above compared to when underfilled. Moving forwards additional hydrogel was used to ensure wells were completely filled

Even with all approaches taken to try eliminating bubbles from the system this was never fully accomplished. However, the viability of the flow organoids was on a comparable level to the control organoids and the flow over the organoids was more uniform and laminar which is important as the type of flow can have an impact on development.

A



B



C

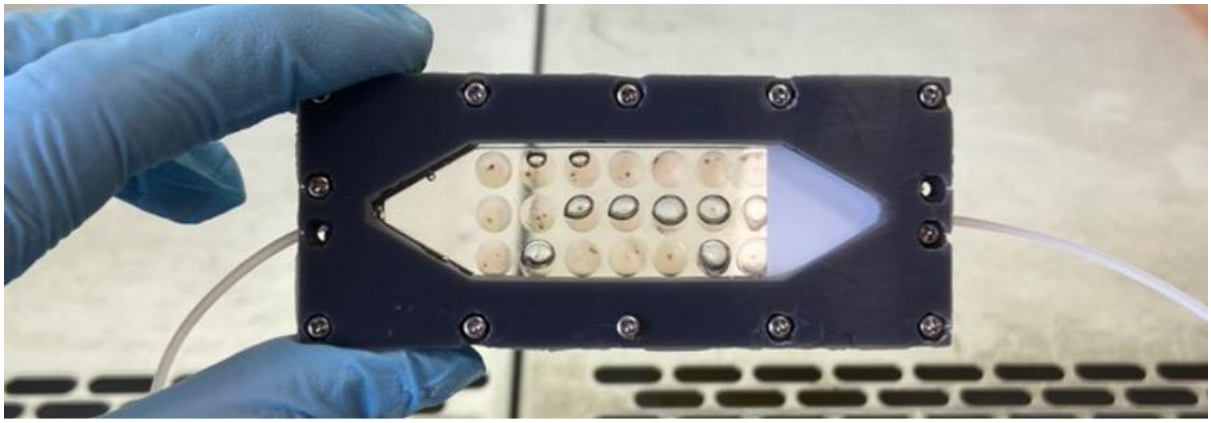


Figure 12. Bubbles formed within the microfluidic chip designs.

(A) Bubble formed from initial microfluidic chip design around the inlet after 3 days of 40µl/min flow. (B) Bubble formed from secondary microfluidic chip design with reduced microwells and channel size after 3 days of flow. (C) Bubbles formed over the 25µl microwells when microwells were not fully filled with hydrogel.

Effect of fluidic flow on the vasculature

Viability of flow vs static

A flow rate of 40µl/min was applied to the organoids for 6 days, from day 7-13 of culture, to coincide with when vasculature sprouting occurs. Organoids were dissociated and stained with annexin V and DAPI to quantify the viability. There is no significant difference between the viability of the control organoids at 73%, compared to the flow treated at 68% and no significant difference in apoptosis in the flow organoids at 15% compared to 12% in control organoids (Fig 13).

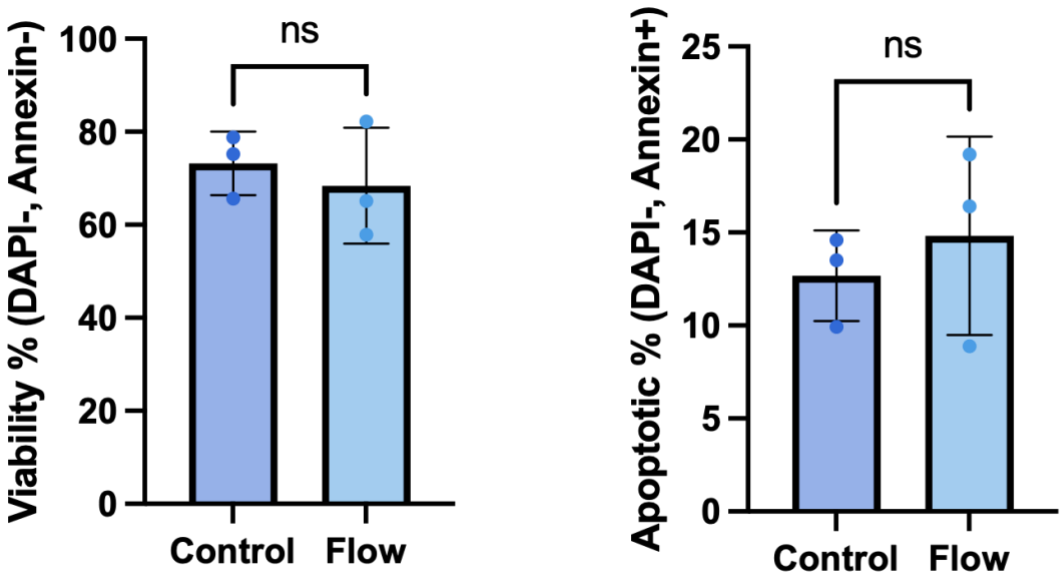


Figure 13. Flow treated organoids are as viable as the control organoids.

Gating strategy from Figure 9 used. Statistical analysis unpaired t test. P value > 0.5, n.s = not significant. N=3 independent experiments.

Changes in the vasculature under fluidic flow

To investigate the effect of fluidic flow upon the vasculature, whole mount imaging was performed. The organoids were stained with anti-VE-cadherin to analyse the vasculature. The vasculature within the control organoid appeared contiguous, as a connected system. Initially the flow-treated organoids were smaller in size overall compared to the control organoids and the vasculature appeared non-contiguous and interrupted (Fig 14A). However, upon further attempts the flow-treated organoids grew in overall size and displayed a connected network of vessels along with the control organoids, likely due to improvements within the protocol and use of fluidic device (Fig 14B). To describe and quantify elements of the vasculature, angiotool analysis was performed on max intensity projection (Z-stack images converted into 2D) images of the vasculature. The parameters of the angiotool were adjusted until an overlay was produced that ensured all vessels were included (Fig 14C). There was no significant difference in the size of the explant area between the control and flow-treated organoids. Initially, from visual observations the flow-treated organoids seemed smaller, and the total cell count was lower, which could

have indicated that some cells are being washed away during the fluidic flow. Upon further attempts, the flow organoids grew, and the cell count increased (Fig 14D).

The total vessel area was greater in the flow treated organoids compared to the control but not significantly. However, the vessel percentage area was significantly less in the flow treated compared to the control organoids, indicating a greater proportion of vessel: organoid in the control organoids (Fig 14E-F). This indicates that the addition of a fluidic flow at 40µl/min did not enhance angiogenesis. CD31 was used as a marker for endothelial cells in the organoids. Upon flow cytometric analysis, two distinct populations were observed with high CD31 and low CD31 expression, indicating two different populations of endothelial cells (Fig 14H). In a single experiment, there appeared to be more of both populations in the control compared to the flow treated organoids. However, the CD31 low population was proportionally greater in both the flow-treated and control organoid compared to the CD31 high (Fig 14G-H).

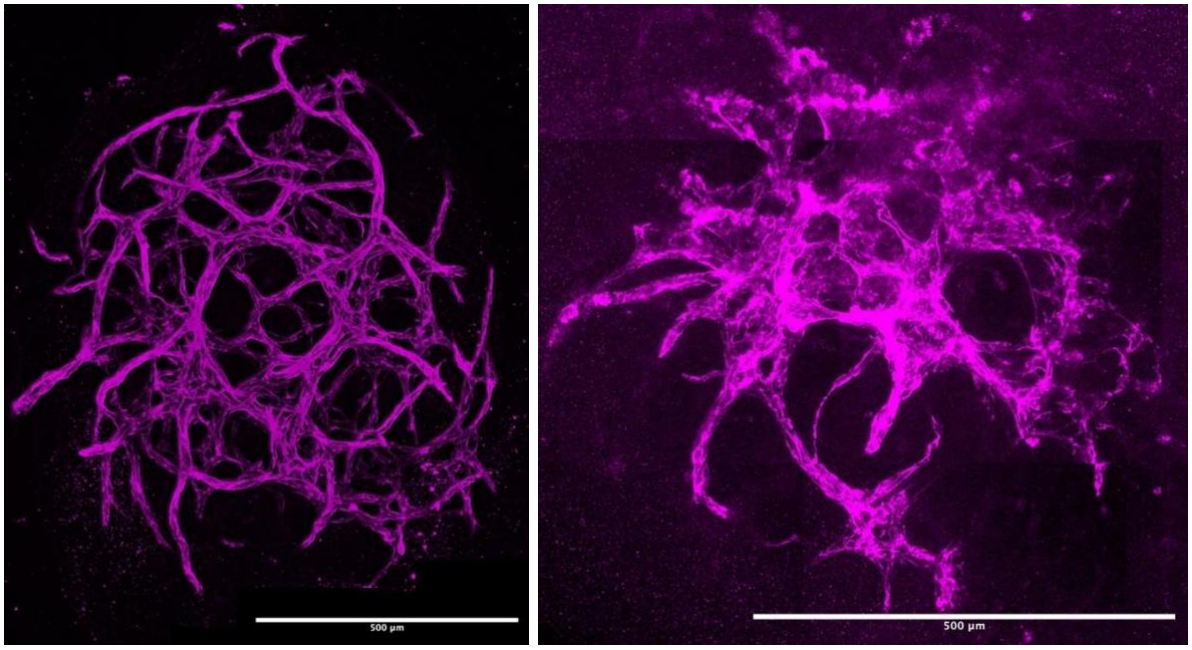
The total number of vessel junctions was not significantly greater in the control compared to the flow treated organoids. However, the junction density was significantly greater in the control compared to the flow-treated organoids indicating less angiogenesis (Fig 14I).

The angiotool analysis indicated that average overall vessel length in the flow-treated organoids was not different to the control as shown in Fig 14J, whilst the average vessel diameter was greater in the flow treated which could indicate different vessels being formed (Fig 14K).

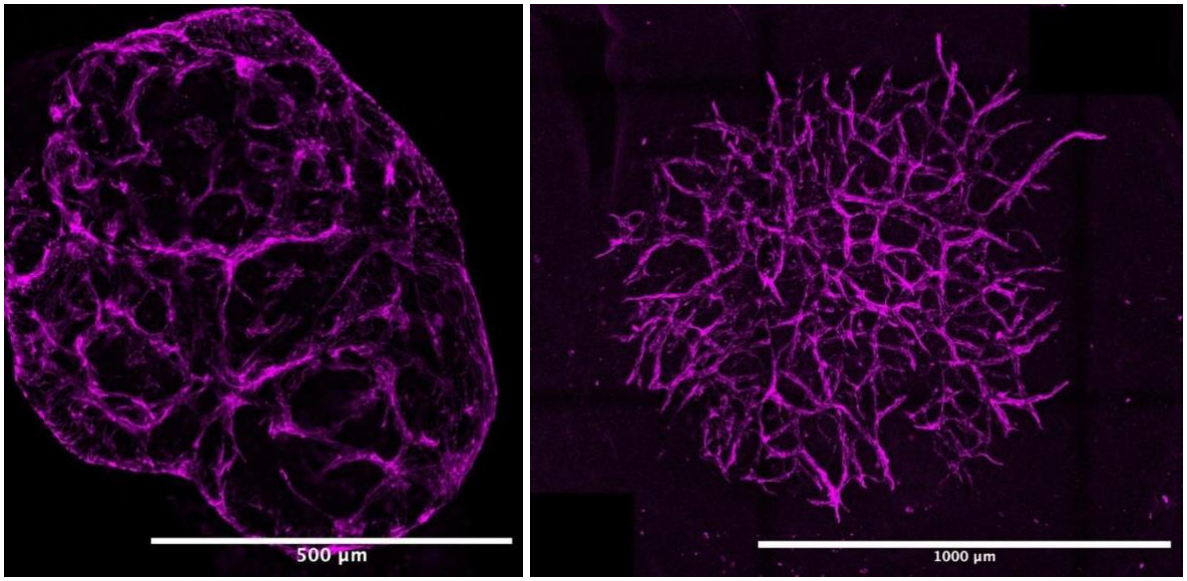
A

Control

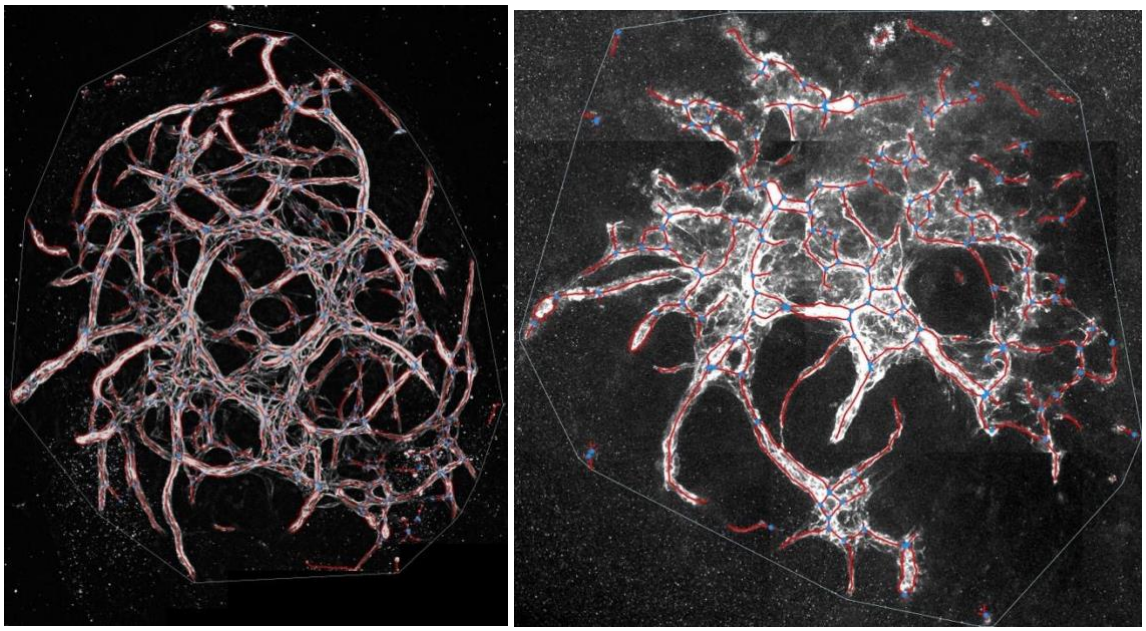
Flow



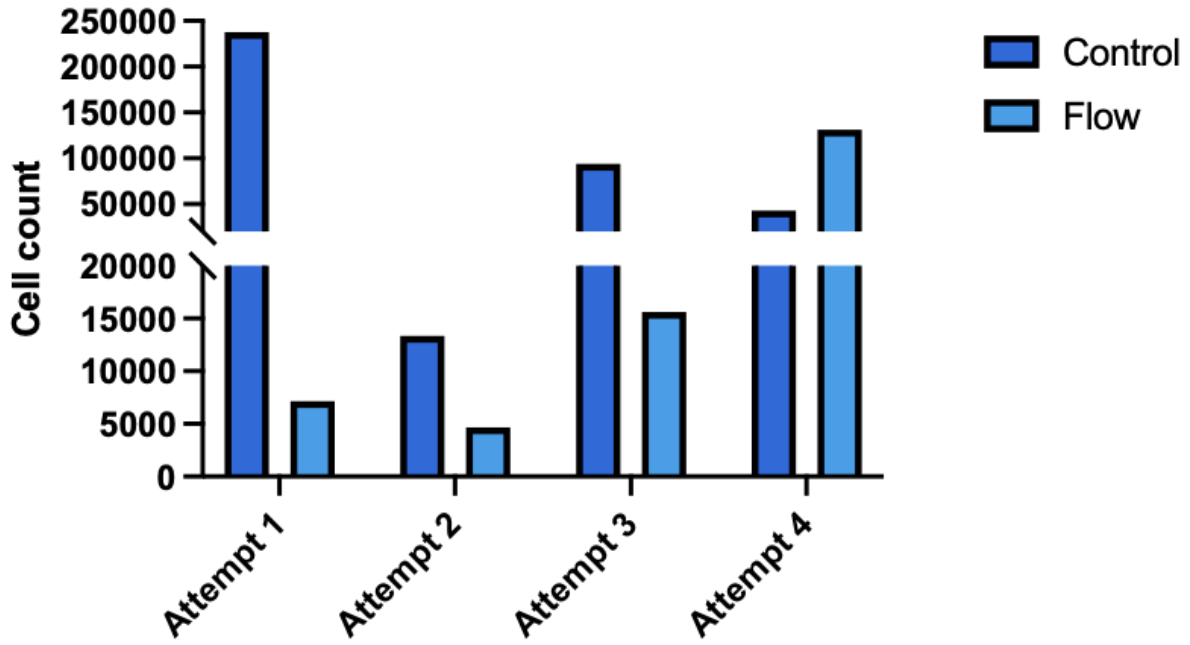
B



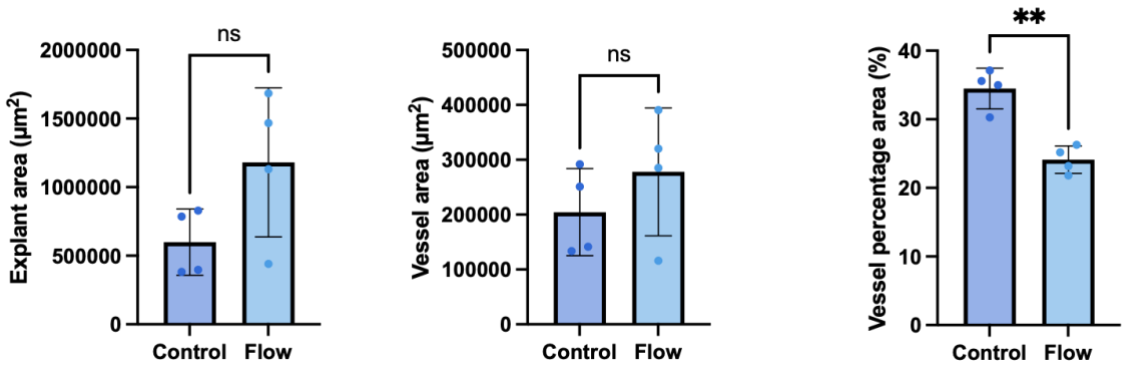
C



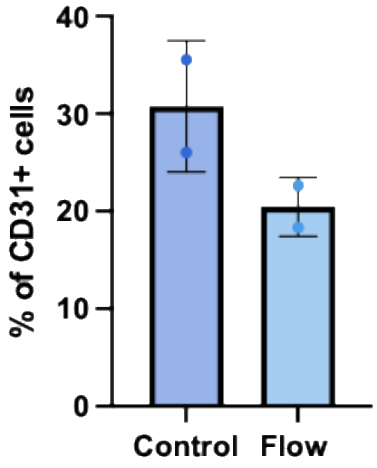
D


Cell count
250000
200000
150000
100000
50000
20000
15000
10000
5000
0
Attempt 1
Attempt 2
Attempt 3
Attempt 4
Control
Flow

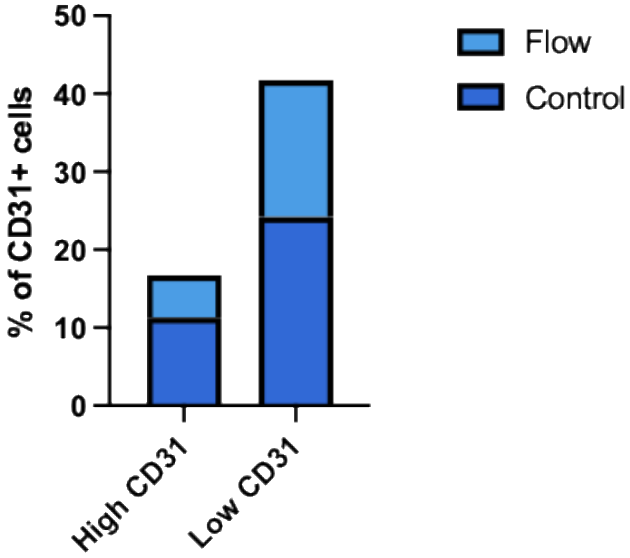
E


ns
Explant area (µm²)
2000000
1500000
1000000
500000
0
Control
Flow
ns
Vessel area (µm²)
500000
400000
300000
200000
100000
0
Control
Flow
**
Vessel percentage area (%)
40
30
20
10
0
Control
Flow

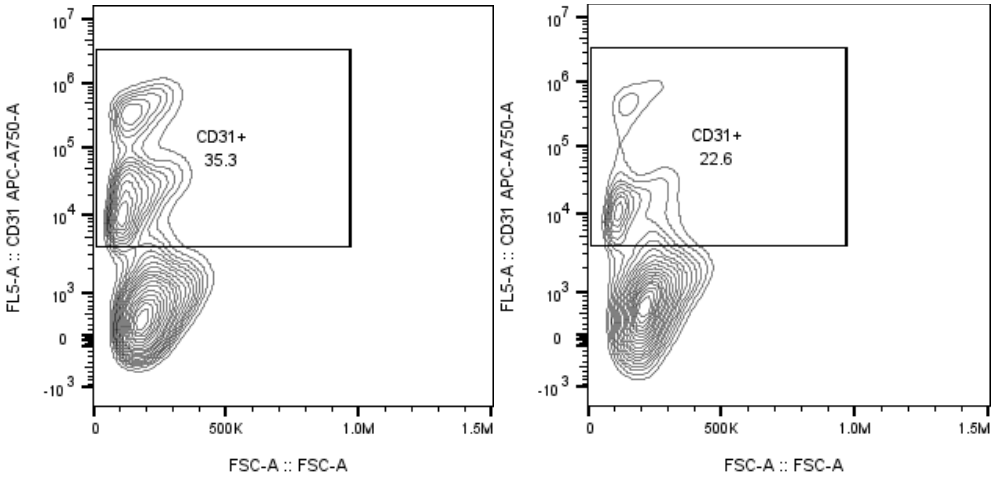
F


% of CD31+ cells
40
30
20
10
0
Control
Flow

G


% of CD31+ cells
50
40
30
20
10
0
High CD31
Low CD31
Flow
Control

H


FL5-A :: CD31 APC-A750-A
CD31+
35.3
FSC-A :: FSC-A
FL5-A :: CD31 APC-A750-A
CD31+
22.6
FSC-A :: FSC-A

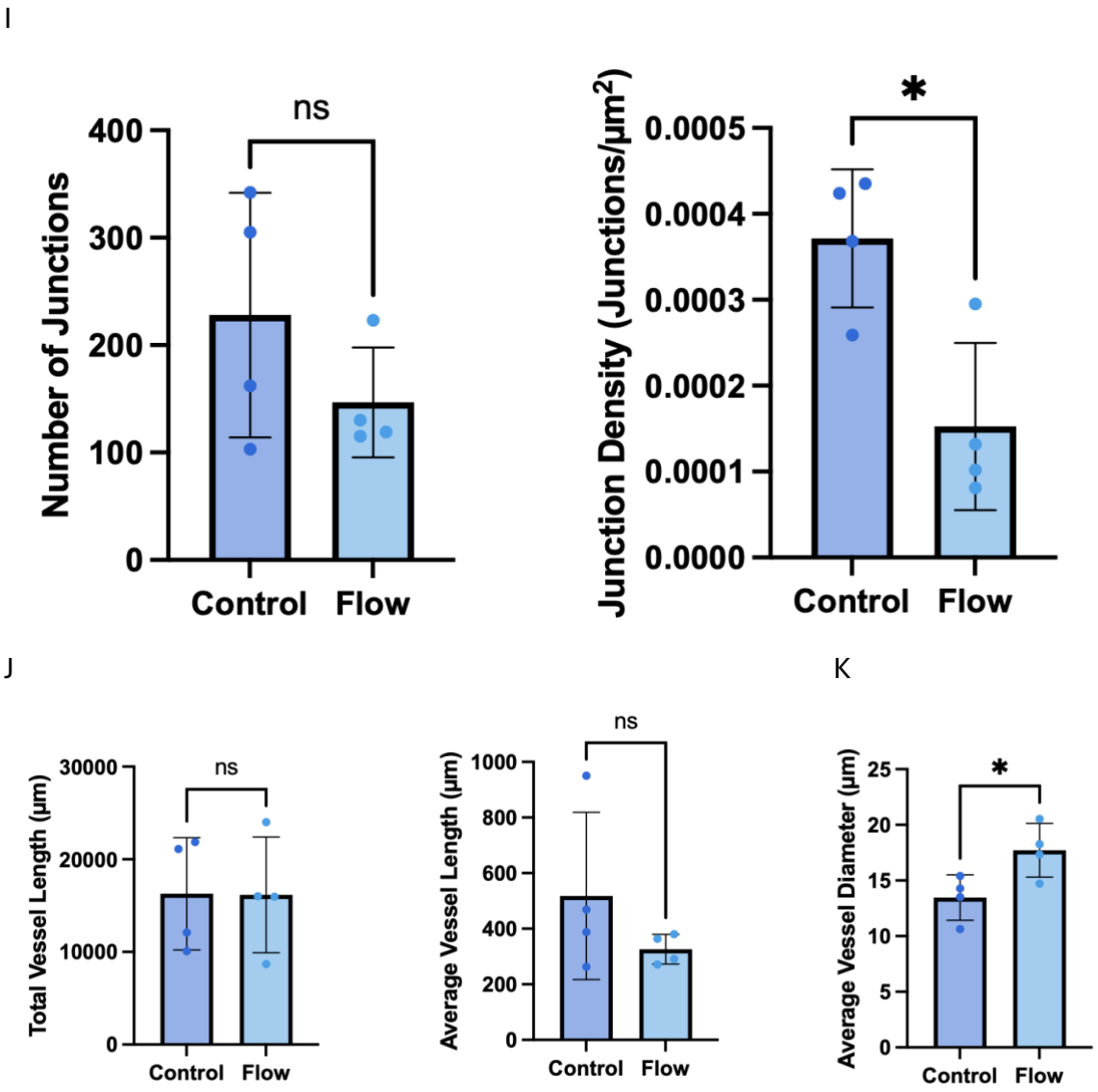


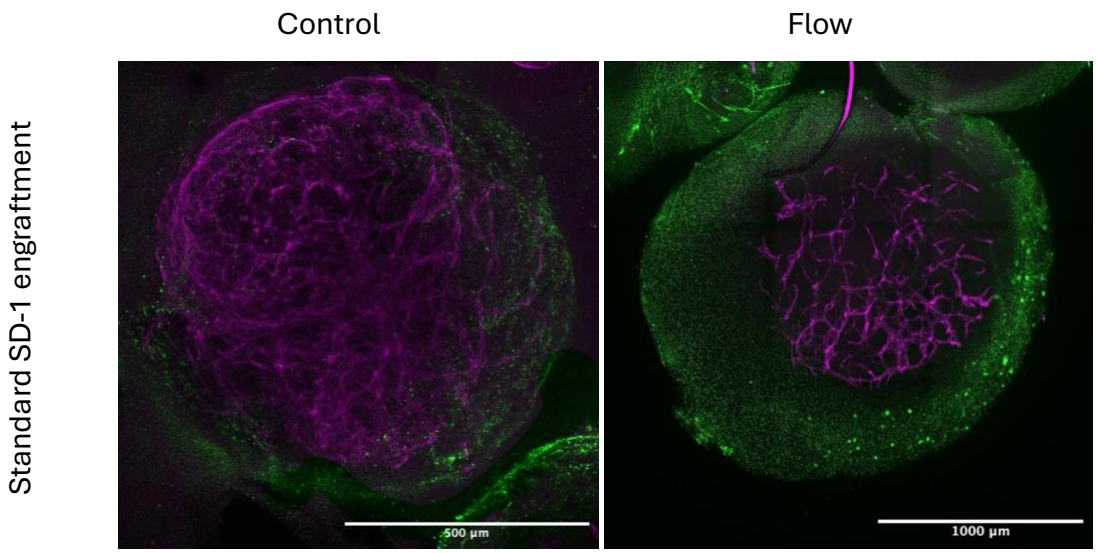
Figure 14. Fluidic flow inhibits vasculature growth in organoids.

*(A) Max intensity of whole mount imaging stained with anti-VE-cadherin (magenta) of control and flow-treated organoid in first attempt. (B) Max intensity of whole mount imaging stained with anti-VE-cadherin (magenta) of control and flow-treated organoid from later attempt. (C) Angiotool overlay of whole mount imaging in Fig 13A. (D) Cell count for control and flow treated organoids determined by flow cytometry for each attempt in microfluidic device. (E-G and I-K) Angiotool analysis, N=4, Unpaired t test, P > 0.05 = ns, P < 0.005 = **, P < 0.05 = *. (E) Explant area µm², Vessel area µm² and Vessel percentage area. (F) Percentage of CD31+ cells in control compared to flow treated organoids N=2. (G) Percentage of CD31+ high compared to CD31+ low in control vs flow treated organoids N=1. (H) Flow plots showing CD31+ population that has two clear high and low populations in the control and flow treated organoids. (I) Number of junctions and*

junction density measured in junctions/μm^2. (J) Total vessel length (μm) and average vessel length (μm). (K) Average vessel diameter (μm)

Effect of fluidic flow on engraftment of ALL in bone marrow organoids

Engraftment of ALL cells into the organoids was primarily in the outer of the organoid and the cells did not penetrate to the centre of the tissue. Standard engraftment was done by adding 6000 SD-1 cells to the phase IV media. I wanted to determine if engraftment through fluidic flow created better engraftment of the ALL cells. On day 14, control organoids were embedded into the microfluidic device, alongside flow organoids and a media with 10,000 SD-1 cells and a fluidic flow of 40μl/min was applied. Whole mount imaging was performed to analyse the engraftment of ALL. The SD-1 cells were stained with anti-CD19 and vessels with anti-VE-cadherin. Images showed that under standard conditions the SD-1 cell engraftment could not penetrate the tissue in the control or flow organoids. In the flow organoids, engraftment was restricted due to SD-1 cells binding to the collagen it was embedded in whilst in the microfluidic device. Under the flow engraftment, there was no improvement in penetration of the SD-1 cells in the control organoids. Similarly to the flow organoid under standard ALL engraftment, the SD-1 cells bound to the collagen instead of the organoid itself. All organoids were washed thoroughly before staining and imaging, but this did not seem to remove the collagen (Fig 15).



SD-1 engraftment through fluidic flow

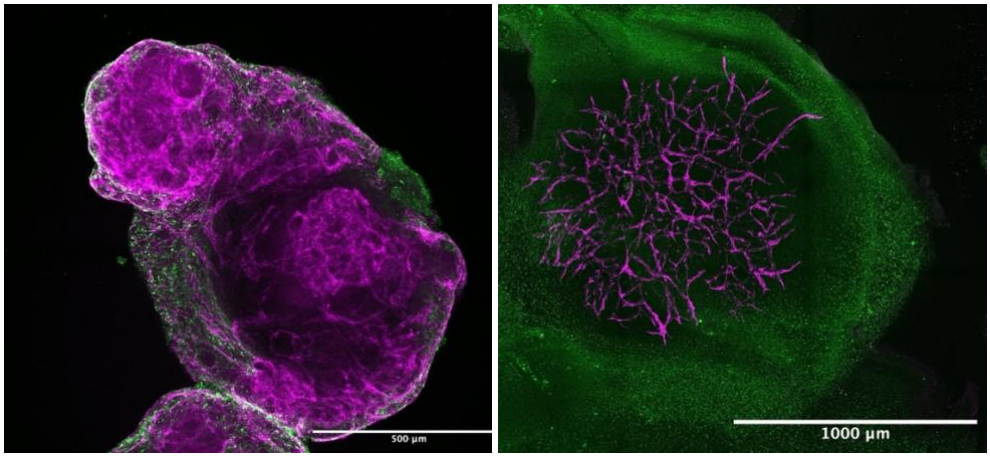


Figure 15. The use of fluidic flow does not improve engraftment of ALL cells in bone marrow organoids.

On day 14 engraftment of ALL was performed in control organoids with with SD-1 engraftment in 96 well plate (standard engraftment) or control organoids were embedded into microfluidic device and SD-1 engraftment was done via a fluidic flow and flow organoids engraftment in the standard SD-1 engraftment or through fluidic flow. Max intensity of whole mount images stained with anti-VE-cadherin (magenta) and anti-CD19 (green). Scale bar = 500µm for control organoids and scale bar = 1000µm for flow-treated organoids.

Modifying IPSC to allow label-free analysis of the vasculature using RFP under control of VE-cadherin promoter

In order to overcome the limitations of antibody staining of the vasculature within the organoids, I began to generate IPSC expressing RFP under the control of the VE-cadherin promoter. Using PrimerBlast, primers for the VE-Cadherin promotor, the miRFP region and a backbone containing the PDGFRB promotor region (Fig 3, Table 3). Initially, a PCR was performed on each primer to ensure the correct region was being amplified. The product was run on a 0.1% agarose gel in 0.25 x TAE for 10 minutes with the appropriate ladder. VE-Cadherin promoter primers were designed with and without overhangs using gDNA, to assist with generation of the plasmid. VE-Cadherin promoter displayed the correct product whilst VE-Cadherin promoter 2 had to be re-run using the PCR product rather than the original gDNA (Fig 16A and 16B), all primer sequences can be found in

table 6. Amplification via PCR was performed using the miRFP promoter and the plasmid backbone. These primers had to be rerun due to the 100bp ladder being visible (Fig 16B). The plasmid backbone was not visible (Fig 16C), which was initial thought to be due to using the wrong annealing temperature. Upon another attempt, the PCR product showed three separate bands. However, it was difficult to determine the size of these bands due to the 1kb ladder used not separating properly (Fig 16D). Further attempts using a different 1Kb ladder showed that none of the bands produced were of the correct 6000bp, which was the expected length of the plasmid backbone promoter (Fig 16E). Due to time limitations, no further actions were taken in the cloning protocol.

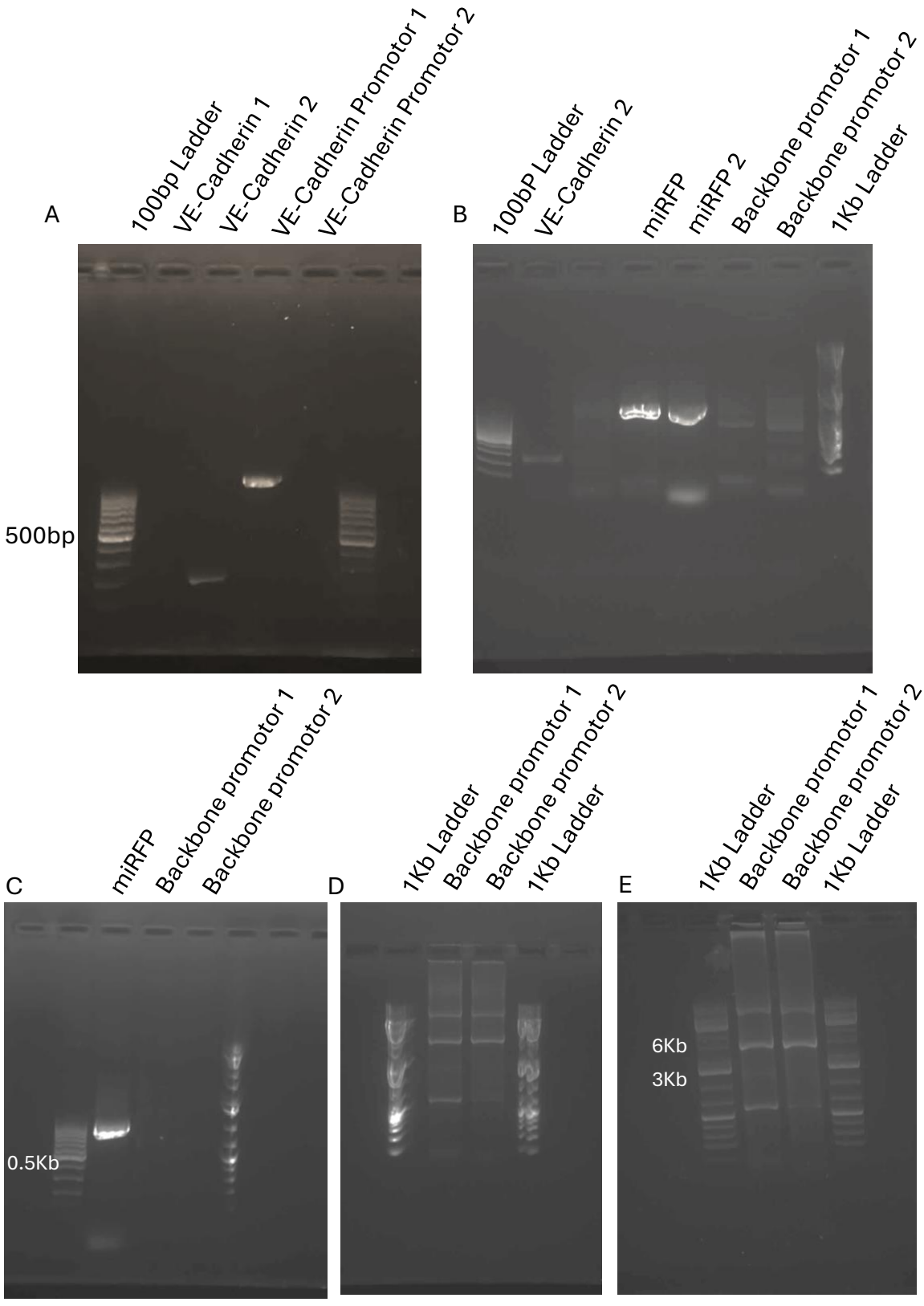

A
100bp Ladder
VE-Cadherin 1
VE-Cadherin 2
VE-Cadherin Promotor 1
VE-Cadherin Promotor 2
500bp
B
100bP Ladder
VE-Cadherin 2
miRFP
miRFP 2
Backbone promotor 1
Backbone promotor 2
1Kb Ladder
C
miRFP
Backbone promotor 1
Backbone promotor 2
0.5Kb
D
1Kb Ladder
Backbone promotor 1
Backbone promotor 2
1Kb Ladder
E
1Kb Ladder
Backbone promotor 1
Backbone promotor 2
1Kb Ladder
6Kb
3Kb

Figure 16. Gel electrophoresis confirms backbone primer is producing incorrect product.

(A) Gel containing VE-cadherin 1, VE-cadherin 2, VE-cadherin promoter 1 and VE-cadherin promoter 2 respectively and a 100bp ladder either side. (B) Gel containing VE-cadherin promoter 2 using the product from previous PCR as the template, MiRFP and the plasmid backbone for promoter 1 and promoter 2. (C) Rerun of miRFP and backbone for promoter 1 and promoter 2. (D and E) Gel of plasmid backbone promoter 1 and 2 with 1Kb ladder

Discussion

This study was designed to analyse the effect of fluidic flow on the vasculature within a bone marrow organoid. The organoids used for this study were designed by Khan *et al*, containing endothelial cells that generated a sinusoidal-like vasculature that was seen as disconnected (Khan et al., 2023).

To analyse the vasculature within the organoid's antibody staining was used. The endothelial is commonly stained with UEA-1, CD34 and CD31. UEA-1 has been shown to be able to penetrate tissue of an average of 300µm depth, as well as being visible in cryosection slices for vascular staining (Hamid et al., 2003). We observed lots of background and even non-viable staining of the vasculature using UEA-1. Background staining could have been due to insufficient blocking or a need of increased washes (Rebelo et al., 2021). Throughout attempts, the number of washes was increased from three to five with PBS-T and there was no difference seen in staining. The blocking was not changed to coincide with all other staining protocols. The absence of a fluorescent signal may have resulted from the lectin failing to bind to the intended target glycans or due to improper storage conditions, such as exposure to temperature or light, this could have quenched the signal and led to loss of lectin functionality (Rebelo et al., 2021). Primarily, CD34 in expressed in early haematopoietic progenitor cells but can also be used as a vascular endothelial cell marker (Traweek et al., 1991). Similarly to UEA-1, it created lots of background autofluorescence and due to the organoid also containing haematopoietic cells, could have resulted in unintended binding targets. The use of VE-

cadherin, also known as CDH5/CD144 was used for further vascular staining. This is a specific endothelial marker that is located as the junctions between endothelial cells. It is a vital marker expressed during angiogenesis, something we were interested in comparing between our control and flow conditions (Vestweber, 2008). Due to limited background autofluorescence and a clear visible vascular, this was the antibody stain for the most effective downstream analysis.

Due to antibody staining being unreliable, the consideration to create a label-free analysis through cloning of the VE-cadherin promoter region in iPSCs was evaluated. Ideally, a plasmid containing a miRFP connected to the VE-cadherin promoter and transfected into iPSCs that could be differentiated into bone marrow organoids. Whilst the miRFP and VE-cadherin promoters were correctly amplified, unfortunately the backbone promoter region to generate the plasmid was being incorrect cut. This is likely due to the design of the primers on NEBuilder. Given additional time, specific promoter backbone primers would have been designed for each VE-cadherin promoter variant. The constructs could then be assembled via Gibson assembly to generate the plasmid of interest. Following transformation into competent bacterial cells, antibiotic sections would facilitate identification of the positive colonies for plasmid isolation. Verified plasmids could be submitted to the sequencing platform Plasmidsaurus before they are transfected into the iPSCs.

In attempt to improve the vasculature, a fluidic flow was applied to the organoids using a microfluidic device. The microfluidic device was made in collaboration with the engineering department at the University of York, taking inspiration from Homan *et al*, who used microfluidics on a kidney organoid to affect the vasculature (Homan et al., 2019). The flow rate used throughout our experiments was 40µl/min. This flow rate was chosen as it showed an impact on the vasculature within the kidney organoids (Homan et al., 2019). but also using a shear stress calculator, a flow rate of 40µl/min within the size of our microfluidic device would create a shear stress of 6.4 dyn/cm^2 which falls within what is experienced by sinusoidal vessels (0.06-11.1dyn/cm^2). However, the flow velocity is measured at 7.41mm/s which is greater than the 0.23±0.22 mm/s experienced by sinusoidal vessels (Bixel et al., 2017). The shear stress experienced by arterial vessels is much greater than sinusoidal at 40.3-86.3 dyn/cm^2. According to a shear stress

calculator, a flow rate of between 252-540µl/min would be needed to produce a shear stress of that magnitude. Another form of flow experienced by vessels is interstitial flow. This has a much slower velocity of between 0.1 and 2µm/s (Swartz and Fleury, 2007) which in our device would be a flow rate of at least 0.001µl/min, which is not viable within our microfluidic device as the peristaltic pump used does not create a flow this slow. If we wanted to achieve such a low flow velocity, the microfluidic device would have to be reduced in size.

Upon visualising the flow organoids, they originally looked smaller than the control organoids. It is possible that the organoids became more compact with the addition of flow. Analysis of the cell count suggested that cells were being washed away during the addition of a fluidic flow. Further attempts saw both an increase in the cell count as well as the size of the flow organoids, which coincided with the addition of hydrogel in which the organoids were embedded into. This hydrogel was added to eliminate space above the microwells for air bubbles to be trapped in, but coincidently it also increased the amount hydrogel available to the organoids to support the generation of not only endothelial cells but stromal and myeloid lineages as well (Khan et al., 2023). This could explain the increase in size and vessel seen in the later batch of flow organoids.

According to the shear stress calculator, the Reynolds number achieved within the device is 1, which would indicate a laminar flow (Freund et al., 2012). However, there are other factors that can affect the type of flow experienced by the organoids, primarily the bubbles that were formed within the system. Initially, the bubbles formed were a problem for the organoids due to a significant reduction in the viability compared to the control organoids. Upon further optimisation the viability became comparable between the two conditions, but the bubbles created additional problems. They obstructed the flow, disrupting the uniform laminar flow that was expected to be generated by the peristaltic pump. A disrupted flow is linked to many vascular diseases as it creates a reduced shear stress that leads to inflammation and apoptosis of endothelial cells. This could explain the reduced vasculature seen in the flow treated organoids. Moreover, a disruption in the flow can also affect the branching points within the vascular network - this was seen in the flow organoids, by a reduced junction density (Chiu and Chien, 2011).

Bubbles were a major issue throughout this study. They may seem small and irrelevant but bubbles in microfluidics can lead to the failure of many biological models, including damage to cells within a microfluidic chamber that in turn leads to changes in morphology (Yang et al., 2022). With optimisation of both the microfluidic device and system they were reduced to where they did not affect the viability of the organoids. Upon first attempts using the microfluidic device an extremely low viability was observed. The combination of understanding the changes being made the protocol, in the context of embedding the organoids individually into the microwells, in addition to the loss of media likely resulted in this low viability. Determining the source of the bubbles present was a combination of air being drawn in when creating a closed system, dissolved gas within the media and released by the organoids during culture. Clamping the end or the tubing, similarly to what is done when blood is being taken to stop air bubbles entering the human bloodstream, was applied to restrict air drawn into the system. Degassing media can be done by placing tubing into an anaerobic chamber to allow equilibration (Plotkin et al., 2018), through addition of heat or using a vacuum. These are all long processes, some that require specialised equipment and all that would require sterilisation of the media afterwards. Therefore, the use of a bubble trap was implemented into the microfluidic system to remove additional bubbles formed throughout culture. The addition of an autoclavable bubble trap did not eliminate bubbles from the system, which has been observed with many bubble traps that have been developed (Huang et al., 2020a) or increase the viability of the organoids. However, it did reduce the number of bubbles to allow for any which were formed to be pushed over the organoids and through the system, rather than being trapped (data not shown). There are still improvements that could be applied to the microfluidic device to eliminate the bubbles, as it is not fully understood the effect they could be having on the morphology or development of the organoids within the system.

Polydimethylsiloxane (PDMS) was used to fabricate the microfluidic device due to its favourable transparency and gas permeability, properties that make it the standard material used in biological microfluidics. Despite these advantages, PDMS can absorb hydrophobic small molecules, including cytokines (Toepke and Beebe, 2006). This could affect the concentration of the media that is used for generation. PDMS has previously

been shown to absorb drugs that has affected drug dosing studies using microfluidics (Grant et al., 2021). During the fluidic phase, the cytokines added include VEGFA and VEGFC that promote vascular development. Even though it is unlikely for the PDMS to absorb these molecules, as they are large, the concentration could have been affected. This in turn could alter the cell behaviour and structure of the overall organoid, as well as the vasculature. An alternative to PDMS is the use of thermoplastics such as polystyrene (PS), cyclic olefin copolymers (COC), and polymethyl methacrylate (PMMA). These materials exhibit several properties that are advantageous for microfluidic applications. These include high mechanical and thermal stability, low water absorption and optical transparency. Nevertheless, each material presents specific limitations: PS is susceptible to degradation upon exposure to ultraviolet (UV) light, whilst PMMA processes high hydrophobicity and low mechanical strength (Rodriguez et al., 2023). Each material has limitations and due to not using our microfluidic device for drug dosage experiments the use of PDMS is unlikely to be influencing the generation of the organoids, the use of a different material for the structure of the microfluidic device is not necessary.

Once we created a device that could develop viable organoids under a flow condition, quantitative analysis was performed to understand the difference between vascular networks. Through the use of the imageJ plugin angiotool, we were able to quantify multiple aspects of the vasculature and compare between the flow and control conditions to make a conclusion on the effect of fluidic flow. Initially, the flow visually showed a decrease in the size but angiotool analysis displayed no change in the explant area, however there was a trend of increased vessel area in the flow treated organoids. When taking into consideration the amount of vasculature within the overall organoid, there was a decrease within the flow organoids that could indicate a decrease in angiogenesis. This decrease in vasculature and angiogenesis was confirmed by a decrease in the endothelial cells (CD31+) present in the flow treated organoids. Further supporting the idea of fluidic flow decreasing angiogenesis, there was a decrease in the junction density within the flow treated organoids. This data suggests that the addition of flow has a negative impact upon angiogenesis.

However, there was an increase in the average diameter of the flow treated organoids and no impact on the overall vessel length or average vessel length. This may indicate a different type of vessel within the flow treated organoid is being formed. Franz-Wiessner characterised the vessels within the organoid as sinusoidal-like through single cell RNA sequencing (Frenz-Wiessner et al., 2024). The average diameter of a sinusoidal vessel in the bone marrow is between 21.2±10.7 which is the displayed by the flow organoid vasculature, whilst the vessels in the control organoids displayed a smaller diameter more similar to that of intermediate capillaries (11.2±1.9) (Bixel et al., 2017). The protein known as platelet endothelial cell adhesion molecule 1 (PECAM1) or CD31 is expressed on endothelial cells and is an indicator or angiogenic and vasculogenic cells (Kim et al., 2010). Flow cytometric analysis of disaggregated organoids demonstrated two distinct CD31 expressing populations: CD31+ low and CD31+ high – both populations were present with both the control and flow treated organoids. The CD31+ low cells likely represent the L-type capillary vessels that correspond to sinusoidal vessels. Whilst the CD31+ high cells likely represent H-type vessels. Whilst both populations were present in the flow treated and control organoids, the trend showed that both the CD31+ high and low populations were greater within the control organoid, which corresponds with further angiotool data that indicates a greater overall vasculature within the control organoid compared to the flow treated. The flow treated organoid showed no increase within either the CD31+ high or low population indicating that the addition of fluidic flow did not promote the generation of a specific vasculature structure (Sivaraj and Adams, 2016). Further experiments looking at the expression of endomucin (EMCN), due to this being highly expressed in H type vessels, would give further insight into the effect fluidic flow is having upon the types of vessels being produced (Liu et al., 2023a).

Whilst the angiotool analysis output allowed for extensive characterisation of the vasculature, it did have its limitations. Many of the outputs, including the diameter, only displayed the average. This resulted in misleading conclusions. Visualisation of the vasculature within the flow treated organoids displayed thicker vessels compared to the control but analysis showed no difference. A more effective and accurate way to portray the vessel diameter would be using a violin plot that displays the diameter of each individual vessel. Unfortunately, the angiotool software does not provide this data,

however another ImageJ plugin called ‘vessel analysis’ does. Vessel analysis can measure both the vessel density and diameter of selected vessels (Said et al., 2019). However, this also has limitations due to the likely introduction of bias when selecting the vessels for analysis. Another tool that could have been used for angiogenesis analysis was endothelial tube formation assay and fibrin bead assay that were later analysed using the imageJ plugin ‘angiogenesis analyser’. This plugin was able to detect junctions and the formation of new vessels (Carpentier et al., 2020). These additional vessel analysers could have been used in conjunction with angiotool to further characterise and validate the vasculature within the bone marrow organoids.

With additional time and resources, the use of single cell RNA sequencing would have allowed for further analysis into the effect of fluidic flow has upon not only the vasculature, but also signalling pathways and differential gene expression (Haque et al., 2017). This could help further validate findings seen through microscopy and flow cytometry. Additionally, the use of immunofluorescence could have been more specific towards distinct types of vessels. A previous study has shown that EphB4 is located on venous endothelial cells, whilst ephrin B2 is located on arterial vessels (Bai et al., 2014). The ability to distinguish between different vessels could help support previous findings that fluidic flow can form different vessel types.

A limitation of the bone marrow organoid model for investigating haematological disease is its ability to engraft B-ALL cells. Currently, the B-ALL cells are unable to penetrate the centre of the organoid. With the addition of a fluidic flow, the engraftment did not improve. A noticeable difference between the flow treated and control organoid was the collagen build up that was not removed from the flow treated organoids upon washes. The B-ALL cells become bound to the collagen instead of penetrating the organoid. It was thought that using the fluidic flow upon the control generated organoid would increase engraftment of the B-ALL but unfortunately the control organoids had to be embedded into the microfluidic system using hydrogel which resulted in an increased collagen layer around the organoid and no improvement of engraftment. In the future, the removal of this collagen layer from around the organoids, using either an enzymatic or mechanical process, could assist with the improvement of B-ALL engraftment with increased depth

into the organoid to generate a more biologically relevant model of haematological diseases.

In conclusion, we successfully generated bone marrow organoids and integrated them into a microfluidic device, developed by Dr Callum Silver in the engineering department, to enable controlled fluidic flow across the organoids. We were able to take the viability of the organoids in our original microfluidic device from 11% to no difference from the control organoids in our final design. An effective antibody, in anti-VE-Cadherin was used for whole mount imaging of that vasculature, that was quantified using the imageJ plugin, angiotool. The addition of a fluidic flow did not positively improve the vasculature within the organoids, with a decrease in angiogenesis displayed. However, it did demonstrate the production of different vessel types, through an increase in the vascular diameter. Further experiments, using different flow rates that align with specific types of vessel structures, could help make more informed conclusions upon the effect of a fluidic flow on the vasculature in bone marrow organoids. Whilst the fluidic flow that was applied did not impact the vasculature within the organoids in the expected way, we were able to establish a model that can be built upon in the future.

Appendix

Appendix 1. Code for whole mount image processing

```
from google.colab import drive
drive.mount('/content/drive')
from PIL import Image
from os import walk
import numpy as np
import tifffile as tf
import os
import pandas as pd



from google.colab import drive
```

```
drive.mount('/content/drive')



import os
import pandas as pd
import numpy as np
import tifffile as tf
from tifffile import TiffWriter

folder = '/content/drive/MyDrive/Mres/Thesis_images3'

if not os.path.exists(folder):
  print(f"Error: The folder '{folder}' was not found. Please check the path.")
else:
  images = [os.path.join(folder, x) for x in os.listdir(folder) if x[-3:] == "tif"]

  sizes = []

  for im in images:
   with tf.TiffFile(im) as tif:
    meta = tif.imagej_metadata
    z_res = meta['spacing']
    z_stack = meta['slices']
    sizes.append([str(im), z_stack, z_res, (z_res*z_stack), 1, 1])

  size_array = np.array(sizes)
  size_df = pd.DataFrame(size_array, columns=['filename', 'z_stack', 'z_res', 'microns',
'z_scale', 'depth_scale'])
  # print(size_df)
  # print(size_array[0])

  min_res = float(size_df['z_res'].max())
```

```
min_size = float(size_df['microns'].min())

for i, row in size_df.iterrows():
 z_scale = min_res // float(row['z_res'])  if min_res > float(row['z_res']) else 1
 depth_dif = float(row['microns']) - float(min_size)
 depth_end = int(row['z_stack']) - (depth_dif // float(row['z_res']))
 with tf.TiffFile(row['filename']) as tifarray:
  array = tifarray.asarray()
  # print(array.shape)
  #### [Z,C,Y,X]
  array = array[:int(depth_end):int(z_scale),:,:,:]
  # print(array.shape)

 output_path = row['filename'][:-4] + '_rescaled.tif'

 with TiffWriter(output_path, imagej=True) as tif:
  tif.write(
     array.astype('uint16'), # Corrected dtype to uint16
     contiguous=True,
     metadata=tifarray.imagej_metadata
  )
```

Abbreviations

BMM	Bone Marrow Microenvironment
MSC	Mesenchymal Stromal Cells
HSC	Haematopoietic Stem Cells
G-CSF	Granulocyte Colony Stimulating Factor
TPO	Thrombopoietin
MPSC	Mesenchymal Progenitor Stem Cells
B-ALL	B Cell Acute Lymphoblastic Leukaemia
ROS	Reactive Oxygen Species
AraC	Cytarabine

α-SMA	α- Smooth Muscle Actin
TNT	Tunnelling Nanotubules
PDX	Patient Derived Xenograft
MRD	Minimal Residual Disease
CAF	Cancer Associated Fibroblast
Mt-dsRNA	Mitochondrial double stranded RNA
EMC	Extracellular Matrix
IPSC	Induced Pluripotent Stem Cells
FGF	Fibroblast Growth Factor
BMP	Bone Morphogenic Protein
GSK3	
scRNA	Single Cell RNA
VEGF	Vascular Endothelial Growth Factor
EMCN	Sialoglycoprotein Endomucin
NO	Nitric Oxide
MAPK	Mitogen- Activated Protein Kinase
NOS	Nitric Oxide Species
Ang-2	Angiopoietin 2
FBS	Fetal Bovine Serum
PDMS	Polydimethylsiloxane
PBS	Phosphate Buffered Saline
PFA	Paraformaldehyde
BSA	Bovine Serum Albumin
RFP	Red Fluorescent Protein
FWD	Forward
REV	Reverse
gDNA	Genomic DNA
UV	Ultraviolet
PS	Polystyrene
COC	Cyclic Olefin Copolymers
PMMA	Polymethyl Methacrylate

References

AHMED, I., CHEN, K. R., NAKAYAMA, H. & GIBSON, L. E. 1998. Cytosine arabinoside-induced vasculitis. *Mayo Clin Proc,* 73**,** 239–42.

AKIL, A., GUTIERREZ-GARCIA, A. K., GUENTER, R., ROSE, J. B., BECK, A. W., CHEN, H. & REN, B. 2021. Notch Signaling in Vascular Endothelial Cells, Angiogenesis, and Tumor Progression: An Update and Prospective. *Front Cell Dev Biol,* 9**,** 642352.

ASCHAUER, J., KLIMEK, M., DONNER, R., LAMMER, J., ROBERTS, P., SCHRANZ, M. & SCHMIDINGER, G. 2024. Non-invasive quantification of corneal vascularization using anterior segment optical coherence tomography angiography. *Scientific Reports,* 14.

BAI, J., WANG, Y. J., LIU, L. & ZHAO, Y. L. 2014. Ephrin B2 and EphB4 selectively mark arterial and venous vessels in cerebral arteriovenous malformation. *J Int Med Res,* 42**,** 405–15.

BIXEL, M. G., KUSUMBE, A. P., RAMASAMY, S. K., SIVARAJ, K. K., BUTZ, S., VESTWEBER, D. & ADAMS, R. H. 2017. Flow Dynamics and HSPC Homing in Bone Marrow Microvessels. *Cell Reports,* 18**,** 1804–1816.

BURT, R., DEY, A., AREF, S., AGUIAR, M., AKARCA, A., BAILEY, K., DAY, W., HOOPER, S., KIRKWOOD, A., KIRSCHNER, K., LEE, S. W., LO CELSO, C., MANJI, J., MANSOUR, M. R., MARAFIOTI, T., MITCHELL, R. J., MUIRHEAD, R. C., NG, K. C. Y., POSPORI, C., PUCCIO, I., ZUBORNE-ALAPI, K., SAHAI, E. & FIELDING, A. K. 2019. Activated stromal cells transfer mitochondria to rescue acute lymphoblastic leukemia cells from oxidative stress. *Blood,* 134**,** 1415–1429.

BURT, R. J., DEY, A., AKARCA, A., ALLEN, H., AMERIKANOU, R., ATKINSON, S., AUTY, D., CHATZIGEROU, J., CUTLER, E., GUERRA-ASSUNCAO, J. A., KIRSCHNER, K., KUMARI, R., MANJI, J., MARAFIOTI, T., WARD, J. & FIELDING, A. K. 2024. Mitochondrial dsRNA from B-ALL cells stimulates mesenchymal stromal cells to become cancer-associated fibroblasts. *Blood Advances,* 8**,** 5696–5709.

BUSSMANN, J., WOLFE, S. A. & SIEKMANN, A. F. 2011. Arterial-venous network formation during brain vascularization involves hemodynamic regulation of chemokine signaling. *Development,* 138**,** 1717–26.

CARPENTIER, G., BERNDT, S., FERRATGE, S., RASBAND, W., CUENDET, M., UZAN, G. & ALBANESE, P. 2020. Angiogenesis Analyzer for ImageJ - A comparative morphometric analysis of "Endothelial Tube Formation Assay" and "Fibrin Bead Assay". *Scientific Reports,* 10.

CERNECKIS, J., CAI, H. & SHI, Y. 2024. Induced pluripotent stem cells (iPSCs): molecular mechanisms of induction and applications. *Signal Transduct Target Ther,* 9**,** 112.

CHIU, J. J. & CHIEN, S. 2011. Effects of disturbed flow on vascular endothelium: pathophysiological basis and clinical perspectives. *Physiol Rev,* 91**,** 327–87.

DORES, G. M., DEVESA, S. S., CURTIS, R. E., LINET, M. S. & MORTON, L. M. 2012. Acute leukemia incidence and patient survival among children and adults in the United States, 2001-2007. *Blood,* 119**,** 34–43.

DUAN, C. W., SHI, J., CHEN, J., WANG, B., YU, Y. H., QIN, X., ZHOU, X. C., CAI, Y. J., LI, Z. Q., ZHANG, F., YIN, M. Z., TAO, Y., MI, J. Q., LI, L. H., ENVER, T., CHEN, G. Q. & HONG, D. L. 2014. Leukemia Propagating Cells Rebuild an Evolving Niche in Response to Therapy. *Cancer Cell,* 25**,** 778–793.

EBINGER, S., ÖZDEMIR, E. Z., ZIEGENHAIN, C., TIEDT, S., ALVES, C. C., GRUNERT, M., DWORZAK, M., LUTZ, C., TURATI, V. A., ENVER, T., HORNY, H. P., SOTLAR, K., PAREKH, S., SPIEKERMANN, K., HIDDEMANN, W., SCHEPERS, A., POLZER, B., KIRSCH, S., HOFFMANN, M., KNAPP, B., HASENAUER, J., PFEIFER, H., PANZER-GRüMAYER, R., ENARD, W., GIRES, O. & JEREMIAS, I. 2016. Characterization of Rare, Dormant, and Therapy-Resistant Cells in Acute Lymphoblastic Leukemia. *Cancer Cell,* 30**,** 849–862.

FIELDING, A. K., RICHARDS, S. M., CHOPRA, R., LAZARUS, H. M., LITZOW, M. R., BUCK, G., DURRANT, I. J., LUGER, S. M., MARKS, D. I., FRANKLIN, I. M., MCMILLAN, A. K., TALLMAN, M. S., ROWE, J. M., GOLDSTONE, A. H., ADU, M. R. C. U. K. & GRP,

E. C. O. 2007. Outcome of 609 adults after relapse of acute lymphoblastic leukemia (ALL); an MRC UKALL12/ECOG 2993 study. *Blood,* 109**,** 944–950.
FRENZ-WIESSNER, S., FAIRLEY, S. D., BUSER, M., GOEK, I., SALEWSKIJ, K., JONSSON, G., ILLIG, D., ZU PUTLITZ, B., PETERSHEIM, D., LI, Y., CHEN, P. H., KALAUZ, M., CONCA, R., STERR, M., GEUDER, J., MIZOGUCHI, Y., MEGENS, R. T. A., LINDER, M. I., KOTLARZ, D., RUDELIUS, M., PENNINGER, J. M., MARR, C. & KLEIN, C. 2024. Generation of complex bone marrow organoids from human induced pluripotent stem cells. *Nature Methods,* 21.
FREUND, J. B., GOETZ, J. G., HILL, K. L. & VERMOT, J. 2012. Fluid flows and forces in development: functions, features and biophysical principles (vol 139, pg 1229, 2012). *Development,* 139**,** 3063–3063.
GALAN-DIEZ, M., CUESTA-DOMINGUEZ, A. & KOUSTENI, S. 2018. The Bone Marrow Microenvironment in Health and Myeloid Malignancy. *Cold Spring Harb Perspect Med,* 8.
GRANT, J., OZKAN, A., OH, C., MAHAJAN, G., PRANTIL-BAUN, R. & INGBER, D. E. 2021. Simulating drug concentrations in PDMS microfluidic organ chips. *Lab Chip,* 21**,** 3509–3519.
GUNTI, S., HOKE, A. T. K., VU, K. P. & LONDON, N. R., JR. 2021. Organoid and Spheroid Tumor Models: Techniques and Applications. *Cancers (Basel),* 13.
HAMID, S. A., DALY, C. & CAMPBELL, S. 2003. Visualization of live endothelial cells ex vivo and in vitro. *Microvasc Res,* 66**,** 159–63.
HAQUE, A., ENGEL, J., TEICHMANN, S. A. & LONNBERG, T. 2017. A practical guide to single-cell RNA-sequencing for biomedical research and clinical applications. *Genome Med,* 9**,** 75.
HOMAN, K. A., GUPTA, N., KROLL, K. T., KOLESKY, D. B., SKYLAR-SCOTT, M., MIYOSHI, T., MAU, D., VALERIUS, M. T., FERRANTE, T., BONVENTRE, J. V., LEWIS, J. A. & MORIZANE, R. 2019. Flow-enhanced vascularization and maturation of kidney organoids in vitro. *Nature Methods,* 16**,** 255–+.
HOU, S., NIU, G., LIU, X., BOURBON, P. M., ZHANG, D., CUI, P., ZHAO, K., ZHAO, D. & ZENG, H. 2021. A novel transcriptional complex on the VE-cadherin promoter regulated the downregulation of VE-cadherin in the Down Syndrome Candidate Region 1 isoform 1L-mediated angiogenesis. *Microvasc Res,* 138**,** 104209.
HU, N. W., RODRIGUEZ, C. D., REY, J. A., ROZENBLUM, M. J., COURTNEY, C. P., BALOGH, P., SARNTINORANONT, M. & MURFEE, W. L. 2022. Estimation of shear stress values along endothelial tip cells past the lumen of capillary sprouts. *Microvascular Research,* 142.
HUANG, C., WIPPOLD, J. A., STRATIS-CULLUM, D. & HAN, A. 2020a. Eliminating air bubble in microfluidic systems utilizing integrated in-line sloped microstructures. *Biomed Microdevices,* 22**,** 76.
HUANG, F. L., LIAO, E. C., LI, C. L., YEN, C. Y. & YU, S. J. 2020b. Pathogenesis of pediatric B-cell acute lymphoblastic leukemia: Molecular pathways and disease treatments. *Oncol Lett,* 20**,** 448–454.
HUGHES, A. M., KUEK, V., KOTECHA, R. S. & CHEUNG, L. C. 2022. The Bone Marrow Microenvironment in B-Cell Development and Malignancy. *Cancers,* 14.
JUSTE-LANAS, Y., HERVAS-RALUY, S., GARCIA-AZNAR, J. M. & GONZALEZ-LOYOLA, A. 2023. Fluid flow to mimic organ function in 3D
models. *Apl Bioengineering,* 7.

KHAN, A. O., RODRIGUEZ-ROMERA, A., REYAT, J. S., OLIJNIK, A. A., COLOMBO, M., WANG, G. L., WEN, W. X., SOUSOS, N., MURPHY, L. C., GRYGIELSKA, B., PERRELLA, G., MAHONY, C. B., LING, R. E., ELLIOTT, N. E., KARALI, C. S., STONE, A. P., KEMBLE, S., CUTLER, E. A., FIELDING, A. K., CROFT, A. P., BASSETT, D., POOLOGASUNDARAMPILLAI, G., ROY, A., GOODING, S., RAYES, J., MACHLUS, K. R. & PSAILA, B. 2023. Human Bone Marrow Organoids for Disease Modeling, Discovery, and Validation of Therapeutic Targets in Hematologic Malignancies. *Cancer Discovery,* 13**,** 364–385.

KIM, H., CHO, H. J., KIM, S. W., LIU, B., CHOI, Y. J., LEE, J., SOHN, Y. D., LEE, M. Y., HOUGE, M. A. & YOON, Y. S. 2010. CD31+ cells represent highly angiogenic and vasculogenic cells in bone marrow: novel role of nonendothelial CD31+ cells in neovascularization and their therapeutic effects on ischemic vascular disease. *Circ Res,* 107**,** 602–14.

LEE, J., PACKARD, R. R. S. & HSIAI, T. K. 2015. Blood flow modulation of vascular dynamics. *Current Opinion in Lipidology,* 26**,** 376–383.

LI, Y. S. J., HAGA, J. H. & CHIEN, S. 2005. Molecular basis of the effects of shear stress on vascular endothelial cells. *Journal of Biomechanics,* 38**,** 1949–1971.

LITZOW, M. R., SUN, Z., MATTISON, R. J., PAIETTA, E. M., ROBERTS, K. G., ZHANG, Y., RACEVSKIS, J., LAZARUS, H. M., ROWE, J. M., ARBER, D. A., WIEDUWILT, M. J., LIEDTKE, M., BERGERON, J., WOOD, B. L., ZHAO, Y., WU, G., CHANG, T. C., ZHANG, W., PRATZ, K. W., DINNER, S. N., FREY, N., GORE, S. D., BHATNAGAR, B., ATALLAH, E. L., UY, G. L., JEYAKUMAR, D., LIN, T. L., WILLMAN, C. L., DEANGELO, D. J., PATEL, S. B., ELLIOTT, M. A., ADVANI, A. S., TZACHANIS, D., VACHHANI, P., BHAVE, R. R., SHARON, E., LITTLE, R. F., ERBA, H. P., STONE, R. M., LUGER, S. M., MULLIGHAN, C. G. & TALLMAN, M. S. 2024. Blinatumomab for MRD-Negative Acute Lymphoblastic Leukemia in Adults. *N Engl J Med,* 391**,** 320–333.

LIU, L. Y., YUAN, W. J. & WANG, J. F. 2010. Mechanisms for osteogenic differentiation of human mesenchymal stem cells induced by fluid shear stress. *Biomechanics and Modeling in Mechanobiology,* 9**,** 659–670.

LIU, X., ZHANG, P., GU, Y., GUO, Q. & LIU, Y. 2023a. Type H vessels: functions in bone development and diseases. *Front Cell Dev Biol,* 11**,** 1236545.

LIU, Z. L., CHEN, H. H., ZHENG, L. L., SUN, L. P. & SHI, L. 2023b. Angiogenic signaling pathways and anti-angiogenic therapy for cancer. *Signal Transduction and Targeted Therapy,* 8.

MéNDEZ-FERRER, S., BONNET, D., STEENSMA, D. P., HASSERJIAN, R. P., GHOBRIAL, I. M., GRIBBEN, J. G., ANDREEFF, M. & KRAUSE, D. S. 2020. Bone marrow niches in haematological malignancies. *Nature Reviews Cancer,* 20**,** 285–298.

MISHRA, A., KAI, R., ATKURU, S., DAI, Y. C., PICCININI, F., PRESHAW, P. M. & SRIRAM, G. 2023. Fluid flow-induced modulation of viability and osteodifferentiation of periodontal ligament stem cell spheroids-on-chip. *Biomaterials Science,* 11**,** 7432–7444.

NG, C. P., HELM, C. L. E. & SWARTZ, M. A. 2004. Interstitial flow differentially stimulates blood and lymphatic endothelial cell morphogenesis in vitro. *Microvascular Research,* 68**,** 258–264.

NICOLI, S., STANDLEY, C., WALKER, P., HURLSTONE, A., FOGARTY, K. E. & LAWSON, N. D. 2010. MicroRNA-mediated integration of haemodynamics and Vegf signalling during angiogenesis. *Nature,* 464**,** 1196–200.

OLIJNIK, A. A., RODRIGUEZ-ROMERA, A., WONG, Z. C., SHEN, Y. Q., REYAT, J. S., JOOSS, N. J., RAYES, J., PSAILA, B. & KHAN, A. O. 2024. Generating human bone marrow organoids for disease modeling and drug discovery. *Nature Protocols,* 19**,** 2117–2146.

PARK, C. S., YOSHIHARA, H., GAO, Q. S., QU, C. X., IACOBUCCI, I., GHATE, P. S., CONNELLY, J. P., PRUETT-MILLER, S. M., WAGNER, B., ROBINSON, C. G., MISHRA, A., PENG, J. M., YANG, L., RANKOVIC, Z., FINKELSTEIN, D., LUGER, S., LITZOW, M., PAIETTA, E. M., HEBBAR, N., VELASQUEZ, M. P. & MULLIGHAN, C. G. 2023. Stromal-induced epithelial-mesenchymal transition induces targetable drug resistance in acute lymphoblastic leukemia. *Cell Reports,* 42.

PLOTKIN, B. J., SIGAR, I. M., SWARTZENDRUBER, J. A. & KAMINSKI, A. 2018. Anaerobic Growth and Maintenance of Mammalian Cell Lines. *J Vis Exp*.

POLAK, R., DE ROOIJ, B., PIETERS, R. & DEN BOER, M. L. 2015. B-cell precursor acute lymphoblastic leukemia cells use tunneling nanotubes to orchestrate their microenvironment. *Blood,* 126**,** 2404–14.

POLAK, R., ZHANG, E. T. & KUO, C. J. 2024. Cancer organoids 2.0: modelling the complexity of the tumour immune microenvironment. *Nat Rev Cancer,* 24**,** 523–539.

PRITT, S. L. & HAMMER, R. E. 2017. The Interplay of Ethics, Animal Welfare, and IACUC Oversight on the Reproducibility of Animal Studies. *Comp Med,* 67**,** 101–105.

PRZYSINDA, A., FENG, W. & LI, G. 2020. Diversity of Organism-Wide and Organ-Specific Endothelial Cells. *Curr Cardiol Rep,* 22**,** 19.

REBELO, A. L., CONTESSOTTO, P., JOYCE, K., KILCOYNE, M. & PANDIT, A. 2021. An optimized protocol for combined fluorescent lectin/immunohistochemistry to characterize tissue-specific glycan distribution in human or rodent tissues. *STAR Protoc,* 2**,** 100237.

ROBERTS, K. G. 2018. Genetics and prognosis of ALL in children vs adults. *Hematology Am Soc Hematol Educ Program,* 2018**,** 137–145.

RODRIGUEZ, C. F., ANDRADE-PEREZ, V., VARGAS, M. C., MANTILLA-OROZCO, A., OSMA, J. F., REYES, L. H. & CRUZ, J. C. 2023. Breaking the clean room barrier: exploring low-cost alternatives for microfluidic devices. *Front Bioeng Biotechnol,* 11**,** 1176557.

SAID, S. S., YIN, H., ELFARNAWANY, M., NONG, Z., O'NEIL, C., LEONG, H., LACEFIELD, J. C., MEQUANINT, K. & PICKERING, J. G. 2019. Fortifying Angiogenesis in Ischemic Muscle with FGF9-Loaded Electrospun Poly(Ester Amide) Fibers. *Adv Healthc Mater,* 8**,** e1801294.

SAORIN, G., CALIGIURI, I. & RIZZOLIO, F. 2023. Microfluidic organoids-on-a-chip: The future of human models. *Seminars in Cell & Developmental Biology,* 144**,** 41–54.

SCHNEIDER, P., DUBUS, I., GOUEL, F., LEGRAND, E., VANNIER, J. P. & VASSE, M. 2011. What role for angiogenesis in childhood acute lymphoblastic leukaemia? *Adv Hematol,* 2011**,** 274628.

SHEN, Y., BENLABIOD, C., RODRIGUEZ-ROMERA, A., WATSON, E., REYAT, J. S., GURASHI, K., ADNAN-AWAD, S., HARGREAVES, R., KEMBLE, S., SMITH, C. G., CROFT, A. P., OPPERMAN, U., JOOSS, N., WONG, Z. C., RAYES, J., MEAD, A. J., ROY, A., GOODING, S., PSAILA, B. & KHAN, A. O. 2025. comBO: A combined human bone and lympho-myeloid bone marrow organoid for pre-clinical modelling of haematopoietic disorders. *bioRxiv***,** 2025.02.16.638505.

SIVARAJ, K. K. & ADAMS, R. H. 2016. Blood vessel formation and function in bone. *Development,* 143**,** 2706–15.
SKELDING, K. A., BARRY, D. L. & LINCZ, L. F. 2025. Modeling the Bone Marrow Microenvironment to Better Understand the Pathogenesis, Progression, and Treatment of Hematological Cancers. *Cancers (Basel),* 17.
SONG, J. W. & MUNN, L. L. 2011. Fluid forces control endothelial sprouting. *Proc Natl Acad Sci U S A,* 108**,** 15342–7.
SONG, M. & FINLEY, S. D. 2018. Mechanistic insight into activation of MAPK signaling by pro-angiogenic factors. *Bmc Systems Biology,* 12.
SUTHERLAND, R. M., MCCREDIE, J. A. & INCH, W. R. 1971. Growth of multicell spheroids in tissue culture as a model of nodular carcinomas. *J Natl Cancer Inst,* 46**,** 113–20.
SWARTZ, M. A. & FLEURY, M. E. 2007. Interstitial flow and its effects in soft tissues. *Annu Rev Biomed Eng,* 9**,** 229–56.
TANG, X. Y., WU, S., WANG, D., CHU, C., HONG, Y., TAO, M., HU, H., XU, M., GUO, X. & LIU, Y. 2022. Human organoids in basic research and clinical applications. *Signal Transduct Target Ther,* 7**,** 168.
TOEPKE, M. W. & BEEBE, D. J. 2006. PDMS absorption of small molecules and consequences in microfluidic applications. *Lab on a Chip,* 6**,** 1484–1486.
TRAVLOS, G. S. 2006. Normal structure, function, and histology of the bone marrow. *Toxicol Pathol,* 34**,** 548–65.
TRAWEEK, S. T., KANDALAFT, P. L., MEHTA, P. & BATTIFORA, H. 1991. The human hematopoietic progenitor cell antigen (CD34) in vascular neoplasia. *Am J Clin Pathol,* 96**,** 25–31.
TRIMM, E. & RED-HORSE, K. 2023. Vascular endothelial cell development and diversity. *Nat Rev Cardiol,* 20**,** 197–210.
VESTWEBER, D. 2008. VE-cadherin: the major endothelial adhesion molecule controlling cellular junctions and blood vessel formation. *Arterioscler Thromb Vasc Biol,* 28**,** 223–32.
WATSON, O., NOVODVORSKY, P., GRAY, C., ROTHMAN, A. M., LAWRIE, A., CROSSMAN, D. C., HAASE, A., MCMAHON, K., GERING, M., VAN EEDEN, F. J. & CHICO, T. J. 2013. Blood flow suppresses vascular Notch signalling via dll4 and is required for angiogenesis in response to hypoxic signalling. *Cardiovasc Res,* 100**,** 252–61.
WINKELMAN, M. A., KIM, D. Y., KAKARLA, S., GRATH, A., SILVIA, N. & DAI, G. H. 2021. Interstitial flow enhances the formation, connectivity, and function of 3D brain microvascular networks generated within a microfluidic device. *Lab on a Chip,* 22**,** 170–192.
YANG, M., SUN, N., LUO, Y., LAI, X., LI, P. & ZHANG, Z. 2022. Emergence of debubblers in microfluidics: A critical review. *Biomicrofluidics,* 16**,** 031503.
YAO, W., LI, Y. B. & DING, G. H. 2012. Interstitial Fluid Flow: The Mechanical Environment of Cells and Foundation of Meridians. *Evidence-Based Complementary and Alternative Medicine,* 2012.
YOU, L. D., COWIN, S. C., SCHAFFLER, M. B. & WEINBAUM, S. 2001. A model for strain amplification in the actin cytoskeleton of osteocytes due to fluid drag on pericellular matrix. *Journal of Biomechanics,* 34**,** 1375–1386.
YUAN, Y. 2019. Shear stress. *Encyclopedia of tissue Engineering and Regenerative Medicine,* 1.

ZHAO, Z. X., CHEN, X. Y., DOWBAJ, A. M., SLJUKIC, A., BRATLIE, K., LIN, L. D., FONG, E. L., BALACHANDER, G. M., CHEN, Z. W., SORAGNI, A., HUCH, M., ZENG, Y. A., WANG, Q. & YU, H. 2022. Organoids. *Nature Reviews Methods Primers,* 2.
ZUDAIRE, E., GAMBARDELLA, L., KURCZ, C. & VERMEREN, S. 2011. A Computational Tool for Quantitative Analysis of Vascular Networks. *Plos One,* 6.